

Diplomarbeit
zur Erlangung des wissenschaftlichen Grades
Diplom-Physiker

Calculation of the Electric Potential for a Neuronal Activity Model in the Brain

vorgelegt von

Fabian Multrus
geboren am 17.02.1989 in Fürth

TECHNISCHE UNIVERSITÄT DRESDEN
INSTITUT FÜR THEORETISCHE PHYSIK
FACHRICHTUNG PHYSIK
FAKULTÄT FÜR MATHEMATIK UND NATURWISSENSCHAFTEN
2014

1. Gutachter: Prof. Dr. Frank Jülicher

2. Gutachter: Prof. Dr. Ivo F. Sbalzarini

Abgabedatum: 31.12.2014

Abstract

In neuroscience the computational simulation of the electromagnetic field in the brain is used for further understanding and analysing of measured neuronal activity. However, with increasing requirements on higher accuracy of realistic head models, the established meshbased methods get more and more computationally expensive. Therefore the aim of this thesis is to use the quasistatic approximation of Maxwell's equations for the formulation of a framework to calculate the electric potential in multiple domains of differing conductivity, while applying a meshfree, particle method, which is known to perform with far superior efficiency in complex geometries compared to their meshbased counterparts. The presented results of this work are the first steps towards a particle based framework, which will not only allow future research upon computational performance, but also the investigation of different model parameters influencing the simulation.

Kurzfassung

In den Neurowissenschaften werden rechnergestützte Simulationen eingesetzt um das Verständnis und die Analyse aufgenommener Daten neuronaler Aktivität zu erweitern. Die wachsenden Anforderungen an die Genauigkeit realistischer Modelle des menschlichen Kopfes führen jedoch zu einem steigenden Rechenaufwand der weit verbreiteten, auf Netzen basierten Ansätze. Daher ist das Ziel dieser Arbeit mithilfe der quasistationären Näherung der Maxwell'schen Gleichungen ein Modell zur Berechnung des elektrischen Potentials in Regionen unterschiedlicher Leitfähigkeit zu erstellen und des weiteren hierfür eine gitterfreie Partikelmethode zu verwenden, von welcher eine effiziente Rechenleistung in komplexen Geometrien bekannt ist. Die präsentierten Ergebnisse stellen die ersten Schritte auf dem Weg zu einem Framework dar, dass auf einer Partikelmethode basiert und welches in Zukunft nicht nur die Untersuchung der Rechenleistung, sondern auch der Einflüsse von verschiedenen Modellparametern auf die Simulation ermöglicht.

Acknowledgements

First and foremost I want to thank Prof. Dr. Frank Jülicher and Prof. Dr. Ivo F. Sbalzarini for the excellent supervision. I really appreciate their commitment and support of my work. Also my thanks are due to Prof. Shu-Chen Li and her group for both providing me experimental data and valuable insight on experimental psychology. Further I am grateful to the whole MOSAIC group, it was a pleasure to work with you. A special thanks goes to George Bourantas for his great support and advice. At any point he would find the time to discuss my newest findings and further options or help me upon difficulties upon the numerical framework. Furthermore, I would like to thank Ömer Demirel, who helped me a lot with the start of my thesis. Another big thanks goes to Lorenz Hauswald, who was never tired of discussions whether it was during my studies or my thesis and whose thoughts on my work always represented an irreplaceable point of view for me. My last thank is to Ulrich Thümmeler and his support of my visualization and plotting efforts.

Contents

1	Monitoring the Brain	1
2	Background, Physical Description, Discretization Scheme	3
2.1	The Physical Description of Electric Brain Activity	3
2.1.1	Phenomenology of Electromagnetic Activity in the Brain	3
2.1.2	Formulation of the <i>forward problem</i>	5
2.2	MRI - EEG: Non-invasive Investigation Methods for the Brain	8
2.2.1	Magnetic Resonance Imaging	8
2.2.2	EEG: Electric Brain Activity Measurement	10
2.3	Discretization and Operator Approximation by Particles . . .	12
2.3.1	Continuum Particle Methods	12
2.3.2	Operator Approximation: the Method of Particle Strength Exchange	14
2.3.3	The Discretization Corrected PSE Operators	16
3	Development of the Forward Model Framework	19
3.1	DCPSE Operator: Construction and Characteristics	19
3.1.1	Exemplary Construction of a DCPSE Operator	19
3.1.2	Parameters of Choice and Operator Convergence . . .	20
3.2	Utilization of the DCPSE Operator for Solving Linear Partial Differential Equations	23
3.2.1	Associated Shape Functions	23
3.2.2	Formulation of Partial Differential Equations with Asso- ciated Shape Functions	24
3.3	Forward Model Framework	26
3.3.1	Single Region and Multi Region Approach for the For- ward Problem	26
3.3.2	Insertion of a Current Source Dipole	28
3.4	Calculating the Electric Potential in Different Geometries . . .	29
3.4.1	Single Region and Multi Region Approach in Comparison	29
3.4.2	Multi Region in 3D Spherical Geometries	32

3.5 MRI Data Segmentation with Freesurfer	35
4 Conclusion and Outlook	37
A Analytic Solution for a Region with Three Subdomains of Constant Conductivity	38
B Selbstständigkeitserklärung	43

List of Figures

2.1	Cross Section of the Brain	4
2.2	Current Model of a Pyramidal Cell	5
2.3	Spin and Magnetic Moment in MRI	9
2.4	MRI Cross Sections	10
2.5	EEG Electrodes Positions	11
2.6	Particle Kernels and Strengths	13
3.1	DCPSE Error Convergence $r = 1$	21
3.2	DCPSE Error Convergence $r = 2$	22
3.3	Region with Subdomains of Constant Conductivity	27
3.4	Multi Region Approach	30
3.5	Single Region Approach	30
3.6	2D Rectangular Domain	31
3.7	Equipotential Lines for 2D Test Geometry	32
3.8	Sphere with Mixed Boundary Conditions	33
3.9	Sphere with Ideal Dipole	34
3.10	Sphere with Physical Dipole	35
3.11	Skull Surface	36
3.12	Brain Surface	36

List of Tables

2.1 MRI Relaxation Times	10
------------------------------------	----

Chapter 1

Monitoring the Brain

How we think and what drives our thoughts has attracted our attentions all along. And for the longest time its exploration was a privilege of thinkers and philosophers. There just seemed to be no tool, no approach for natural science to observe the activity of our brains. This however started to change in the 1920s, when the discovery and actual measurement of brain electric activity was made by the German physician Hans Berger [1]. At first the progress made was slow, because no one would believe in the results, but in the second half of 20th century this rapidly changed. Especially newly developed investigation methods for such complex organs like the human brain made the difference and helped to create a whole new discipline in neuroscience. Whereas it is a fascinating topic and the interest is growing fast, our knowledge about neuronal processes remains limited until today. A key factor persists, that the capabilities of *in vitro* brain research are very limited. Thus the need for diagnostic methods arises, which provide *in vivo* studies as well as being non invasive.

Several such methods for observing were and still are developed today. Among them are imaging techniques like Magnet Resonance Imaging (MRI) and electromagnetic monitoring of neuronal activities in Electroencephalography (EEG) and Magnetoencephalography (MEG). Whereas MRI gives information about the tissue type and distribution in the human body, EEG and MEG aim to measure the electric potential or magnetic field of biophysical processes. Additionally, these observation methods can benefit from each other. An area of interest, where the combination of MRI and EEG/MEG has been successfully deployed, is in the field commonly denoted as *source localization*. It deals with the problem of locating the origin of the electromagnetic sources and therefore aims to determine the origin of the associated neuronal process to a measurement in EEG or MEG data. This task, however, remains a challenging process and it is of high interest for the neuroscientific community to steadily improve the tools applied to solve this problem.

For *source localization* two approaches are distinguished. On the one hand there is the *inverse problem*, where one directly tries to approximate the source configuration of a given EEG/MEG-dataset and on the other hand the *forward problem*, in which the arising electromagnetic fields are calculated from a known source. Whereas the first one seems to be the intuitive choice to solve this problem, it possesses a key issue. Since the electric potential in EEG is only known on the scalp, any potential distributions on the surface have inherently an infinitely large number of possible source configurations. This leads to the *inverse problem* being generally ill-posed. In comparison the forward problem is well-posed and can also be used for *source localization* inside a Bayesian solver [2]. In addition a forward model has the advantage of allowing to investigate the sensitivity of the problem to different parameters and model assumptions. For example the conductivity values of the brain tissues are not known precisely from experiments and also are not very reliable. Here, the impact of uncertainties on the solution could be demonstrated with help of a forward model. Therefore such a model provides one more powerful tool to improve our knowledge about assumptions of the physical description.

Since an important part of the *forward problem* is the underlying head model, recent research focuses increasingly on the utilization of MRI data to construct realistic shaped head models. This, however, leaves the mainly used mesh-based frameworks as a computationally very inefficient choice. At this point meshless methods can step in and try to satisfy the high requirements put on the accuracy of the simulation, while simultaneously keeping the level of the computational cost reasonable. Particle methods are mesh-free approaches and it is well known from smoothed particle hydrodynamics and vortex methods, that they perform with far superior efficiency in complex geometries compared to their mesh-based counterparts.

In this work the Discretization Corrected Particle Strength Exchange (DCPSE) framework, which bases on a particle discretization scheme, is used to develop a simulation for the electric potential, modeling electric brain activity. Special attention has been paid to an easy and efficient extension to realistic head geometries. In addition, realistic head geometries have been constructed from MRI data for a future possible validation of the simulation.

The first section provides theoretical as well as experimental background of the neurophysiological phenomena and in the second section the concepts of the implemented forward model are presented as well. The concluding section contains a critical analysis of the results and ends up with a summary as well as an outlook on topics worth studying further.

Chapter 2

Neurophysical Background, its Physical Description and a Particle Discretization Scheme

2.1 The Physical Description of Electric Brain Activity

The *source localization* from EEG signals became a growing and important part of nowadays neurological research. However, reconstructing the electric source of neuronal activity remains a challenging task, due to the *inverse problem* being ill-posed. Therefore the well-posed *forward problem* provides an interesting additional approach to study. It can not only be used to localize the sources in EEG, it can also be applied to construct a forward model, which can provide a further investigation tool in form of a computer simulation. This section contains an overview of the underlying neurophysiological phenomena of the *forward problem*, followed by the description in terms of the governing electromagnetic equations and concludes with a partial differential equation (PDE) to solve the *forward problem*.

2.1.1 Phenomenology of Electromagnetic Activity in the Brain

The electromagnetically active regions of the brain relevant for EEG are thought to be mostly located in the cerebral cortex. This outermost layer is giving the brain its characteristic shape due to the folded structure, see Figure 2.1, with its main tissue component being grey matter. Inside this layer far more than 10^{10} neurons exist and most of them are pyramidal cells [3]. This type of cells is perpendicularly

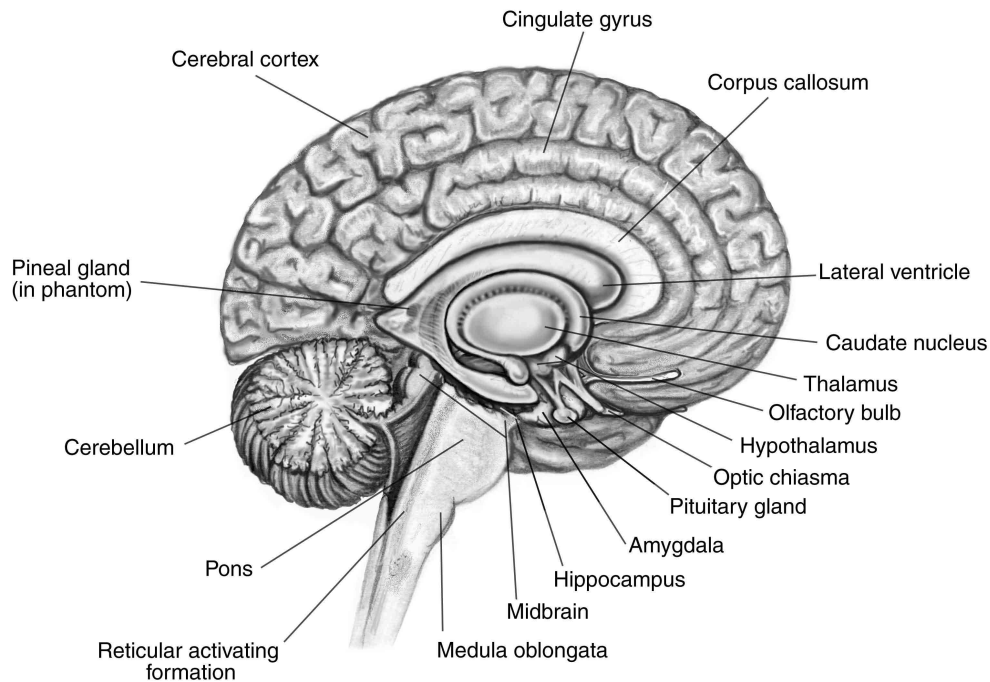


Figure 2.1: Cross section of the Brain [4]

orientated to the cortical surface and their activity is believed to be the origin of the main EEG and MEG signal.

Such a neuronal cell is organized in three parts, the cell body (the soma) including the nucleus, the dendrites and the axon. The dendrites are branching tree-like cell extensions, which are connected to neighbouring neurons, i.e. a synapse, and in general function as receiver for input stimuli. Whereas axons, long fibre-type elements of neuronal cells, can transfer these impulses without any signal losses along their direction. The electrophysiology of this cell level signalling process is highly complex and here only the most important aspects will be outlined. For a more detailed biochemical description see Hämäläinen et al. [3] or Zschocke et al. [5]. A more general overview is provided in Baillet et al. [2].

However, it is useful to imagine the process in a single neuronal cell only in terms of changes in the resting potential of cell membranes [5]. Then an incoming signal at the apical dendrites will lead to an electro-negative excitement of the potential, the so called excitatory postsynaptic potential (EPSP), with respect to the cell body and the basal dendrites. And this potential difference between both ends of the cell, gives rise to a current, flowing from the apical to the basal dendrites (cf. [2]). The two parts of the total current are conveniently denoted as the primary current, directly located between source and sink, and the volume

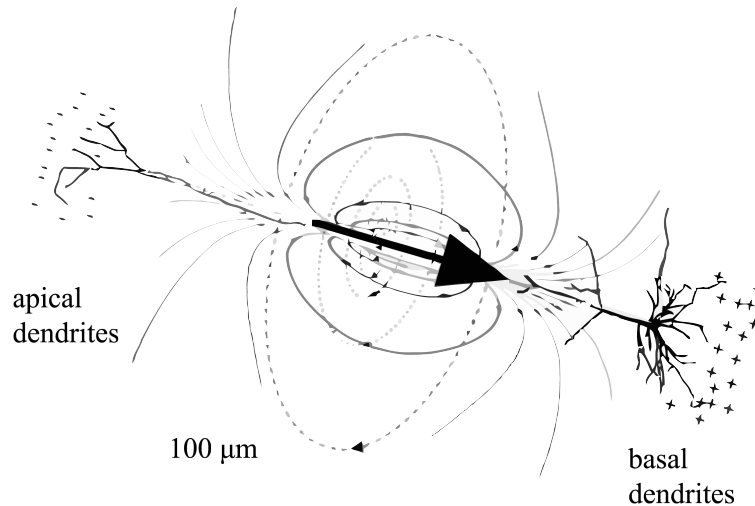


Figure 2.2: Schematic description of an active pyramidal cell with a primary current flow (big arrow), existing between a source (apical dendrites) and a sink (basal dendrites). The solid lines with arrows symbolize the volumetric current, the dotted lines show the induced magnetic field. [6]

current, summing up all the remaining currents flowing in the whole head. It is important to state, that the source and the sink are of the same magnitude, so that no additional currents are created or destroyed. Finally the total current causes an electric as well as a magnetic field throughout the head, see Figure 2.2.

Since the signal produced from a single pyramidal cell is far too small for the finally measurable output of MEG or EEG [3], not single neuronal cells are thought to be the origin of the source, but rather the simultaneous activation of several hundreds to thousands of these. These cell assemblies are called cortical columns and the current flowing inside an active column is believed to be the main contributor to MEG and EEG signals.

2.1.2 Formulation of the *forward problem*

From the physical point of view, the EEG *forward problem* deals with the macroscopic formulation of Maxwell's equations

$$\begin{aligned} \nabla \cdot \mathbf{D}(\mathbf{x}, t) &= \rho(\mathbf{x}, t), & \nabla \cdot \mathbf{B}(\mathbf{x}, t) &= 0, \\ \nabla \times \mathbf{E}(\mathbf{x}, t) &= -\dot{\mathbf{B}}(\mathbf{x}, t), & \nabla \times \mathbf{H}(\mathbf{x}, t) &= \mathbf{J}(\mathbf{x}, t) + \dot{\mathbf{D}}(\mathbf{x}, t). \end{aligned}$$

In this four fundamental equations \mathbf{E} is the electric field and \mathbf{H} is the magnetic field, while the magnetic induction or field density is described with \mathbf{B} and \mathbf{D} is the displacement field. Moreover, the charge density is denoted with ρ and the total current density with \mathbf{J} . The dot upon a vector field symbolizes the partial

derivative in time.

Two major assumptions are made to solve the *forward problem*. On the one hand that Maxwell's equations satisfy the quasistatic approximation and on the other hand that the values of conductivity in each tissue segment are constant and therefore the conductivity field in the head is piecewise constant.

Quasistatic Approximation of Maxwell's Equations A sufficient assumption for the *forward problem* is that the finite velocity of the electromagnetic waves can be neglected. In other words the considered system, here the head, is small in comparison to the wavelength and therefore the fields inside the head can be treated like they would spread out instantaneously [7]. In this case the time derivative dependent terms in Maxwell's equations are small with respect to the remaining ones and can be left out from the further considerations. A detailed evaluation of the quasistatic approximation of the *forward problem* due to the low frequencies and the problem specific conductivity values of the brain tissue are provided in Hämäläinen et al. [3].

The Maxwell equations without time derivative terms are

$$\begin{aligned}\nabla \cdot \mathbf{D}(\mathbf{x}) &= \rho(\mathbf{x}), \\ \nabla \cdot \mathbf{B}(\mathbf{x}) &= 0, \\ \nabla \times \mathbf{E}(\mathbf{x}) &= 0, \end{aligned} \tag{2.1}$$

$$\nabla \times \mathbf{H}(\mathbf{x}) = \mathbf{J}(\mathbf{x}). \tag{2.2}$$

From this equations one important conclusion can be made. Since the curl of $\mathbf{E}(\mathbf{x})$ vanishes in Eq. 2.1, the electric field can be written in terms of a scalar potential $\phi(\mathbf{x})$

$$\mathbf{E} = -\nabla\phi.$$

Current Source Dipole Further $\mathbf{J}(\mathbf{x})$ names in general the total current density, and is assumed to be in a stationary state for the considered neuronal activity. This is appropriate, because the change of the flowing currents relevant for EEG is slow [5]. In the volume of interest V the current density has to be conserved. Since the physical model consists of a current source and a current sink, it is useful to introduce a source density $s(\mathbf{x})$. It is defined with an integral over a volume V and this has to be equal to the size of the fluxes through its interface. In this case, because the sink and the source are of the same magnitude, it is zero

$$\int_{\partial V} \mathbf{J}d\mathbf{A} = \int_V s dV = 0.$$

From this equation it follows with the aid of the divergence theorem that

$$\nabla \mathbf{J}(\mathbf{x}) = s(\mathbf{x}). \quad (2.3)$$

Furthermore one can use Ohm's law to express $\mathbf{J}(\mathbf{x})$ in terms of the electric field $\mathbf{E}(\mathbf{x})$, therefore the electric potential $\phi(\mathbf{x})$, and the conductivity tensor $\underline{\underline{\sigma}}(\mathbf{x})$ for anisotropic media

$$\mathbf{J}(\mathbf{x}) = \underline{\underline{\sigma}}(\mathbf{x})\mathbf{E}(\mathbf{x}) = -\underline{\underline{\sigma}}(\mathbf{x})\nabla\phi(\mathbf{x}). \quad (2.4)$$

Applying Eq. 2.3 in Eq. 2.4 and assuming isotropic conductivity, i.e. the anisotropic conductivity tensor field reduces to a scalar field $\underline{\underline{\sigma}}(\mathbf{x}) \rightarrow \sigma(\mathbf{x})$, this yields the equation to solve the EEG *forward problem*

$$\nabla \cdot (\sigma(\mathbf{x})\nabla\phi(\mathbf{x})) = -s(\mathbf{x}). \quad (2.5)$$

Although the tissues in the head are certainly not isotropically conductive, it is a sufficient assumption for first considerations.

In medical literature the derivation of formula 2.5 often contains the split of the total current into two parts of distinct physiological meaning. The primary current flow $\mathbf{J}_p(\mathbf{x})$ relates to the immediate neuronal activity and the secondary or volumetric current flow $\mathbf{J}_v(\mathbf{x})$ reflects the effect of the electric field on the cell-surrounding charge carriers

$$\mathbf{J}_{tot}(\mathbf{x}) = \mathbf{J}_p(\mathbf{x}) + \mathbf{J}_v(\mathbf{x}). \quad (2.6)$$

Then it is assumed, that the total current density is divergence free $\nabla \mathbf{J}_{tot}(\mathbf{x}) = 0$ without constricting the conservation of the total current density to a control volume V . There Ohm's law (2.4) is only applied for $\mathbf{J}_v(\mathbf{x})$ and one obtains an equation, quite similar to Eq. 2.5, it is

$$\nabla \cdot (\sigma(\mathbf{x})\nabla\phi(\mathbf{x})) = \nabla \mathbf{J}_p(\mathbf{x}).$$

Then $\nabla \mathbf{J}_p(\mathbf{x})$ represents a current source term, but what can get lost in this picture, that the total current $\mathbf{J}_{tot}(\mathbf{x})$ as a whole is contributing to the electric potential and not just the volumetric part $\mathbf{J}_v(\mathbf{x})$.

Ideal Current Source Dipole A commonly used concept to approximate the source density is, with the aid of an ideal or mathematical current dipole

$$s_d(\mathbf{x}) = -\mathbf{I}_d \nabla \delta(\mathbf{x} - \mathbf{x}_d). \quad (2.7)$$

Here \mathbf{I}_d is the current source dipole moment, which relates to the term from the current multipole expansion, see [8], and $\delta(\mathbf{x} - \mathbf{x}_d)$ is the delta distribution, which states the position of the current dipole at \mathbf{x}_d . That an ideal current dipole is an appropriate model for neuronal activity was also demonstrated by Munck et al. [9] and is not to be confused with a charge dipole. The confusion is increased by some literature on this topic, because it does not distinguish consistently the analogy between electric and current source dipoles.

2.2 MRI - EEG: Non-invasive Investigation Methods for the Brain

An important and technologically demanding aspect is to study biological systems in vivo. It becomes even more challenging, if the object of interest is a complex organ like the brain. Especially if one is interested in studying the functionality of brain processes, there is the need for non-invasive diagnostic methods, caused by both experimental and ethical reasons. This led to the development of several new techniques over the last century, like MRI, EEG, Positron Emission Tomography or X-Ray Computed Tomography, to name only a few. Since its introduction in the 1980s, MRI emerged as an important imaging method for modern medicine. EEG on the other hand is a long time diagnosis method and a clinical standard with extensive use, e.g. in the study of epilepsy. In the following sections MRI and EEG will be introduced, starting with a conceptual and physical overview on MRI as well as EEG and ending by taking a look at the synergy of both methods in correlation experiments.

2.2.1 Magnetic Resonance Imaging

In contrast to most medical imaging applications, the MRI working principle is based on nuclear magnetic resonance of hydrogen atoms and so no ionizing radiation is used. This underlying physical phenomenon is of quantum mechanical nature and applies to more than just hydrogen atoms, but its high concentration in the human body makes it the chemical element of choice in modern medical MRI. Here only the physics will be briefly summed up. For more technical details the following books are emphasised [10], [11], [12].

If an external magnetic field \mathbf{B}_0 is applied, in MRI they are usually up to 3 Tesla [10], it will have two impacts on the nuclear spins. First, whenever a spin is not in the direction of \mathbf{B}_0 , e.g. the z -direction, it will undergo precession with a characteristic frequency called Lamor frequency, which only depends on the

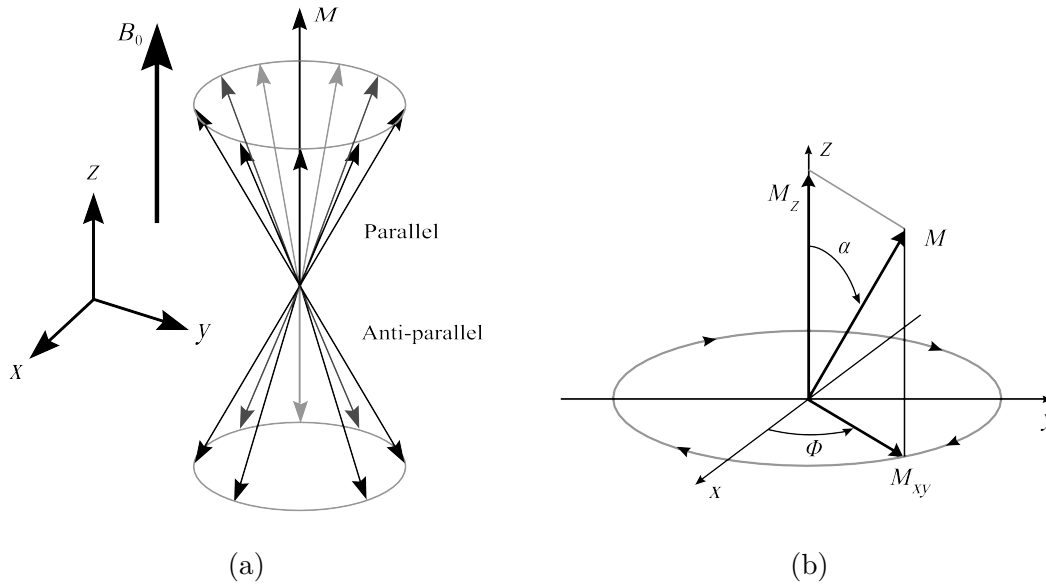


Figure 2.3: a) Spin precession inside an external applied magnetic field \mathbf{B}_0 . More spins will be aligned parallel with respect to \mathbf{B}_0 . [13]

b) \mathbf{M}_{xy} and \mathbf{M}_z portions of the magnetic moment, \mathbf{M}_{xy} will precess around the z-axis, the direction of the applied magnetic field \mathbf{B}_0 . [14]

magnitude of \mathbf{B}_0 and the gyromagnetic ratio γ

$$\omega = -\gamma \cdot |\mathbf{B}_0|.$$

Thus it is possible to distinguish different kinds of atoms, due to their characteristic gyromagnetic ratios, e.g. for protons γ is $42.58 \frac{\text{MHz}}{\text{T}}$ and the resulting Larmor frequency ω is to 63.9 MHz.

And second, over time all spins will align in direction of the magnetic field, whereas the alignment in the same orientation, in this case $+z$, is energetically slightly favoured, see Figure 2.3a. This small difference represents the actually measurable quantity, the net magnetization \mathbf{M}_z , which, in MRI literature, is often referred to as net magnetization vector (NVM). To produce the MRI-signal, in addition to the static magnetic field a radio frequency (RF) pulse excites the atoms in a way that the NVM will be located perpendicularly to \mathbf{B}_0 in the xy -plane. The transverse magnetization \mathbf{M}_{xy} will start to precess about the z-axis, which is shown in Figure 2.3b and therefore induce an alternating voltage in a receiver coil. This is the MRI signal. After the system receiving the RF pulse, the MRI-signal will fade out in characteristic time spans. This is due to the realignment of the excited spins to the z-axis. There are two relaxation times to be distinguished, longitudinal relaxation or T1 recovery and transverse relaxation or T2 recovery. Both of them describe the decay of \mathbf{M}_{xy} , however for different reasons. Whereas the T1 decay is caused by spin-lattice interactions, the T2 decay is attributed to

Tissue	T1 Recovery [ms]	T2 Recovery [ms]
Fat	192	108
White Matter	687	107
Grey Matter	825	110

Table 2.1: Relaxation times T1, T2, at 40° C and $B_0 = 0.5$ T and $\omega_L = 20$ MHz

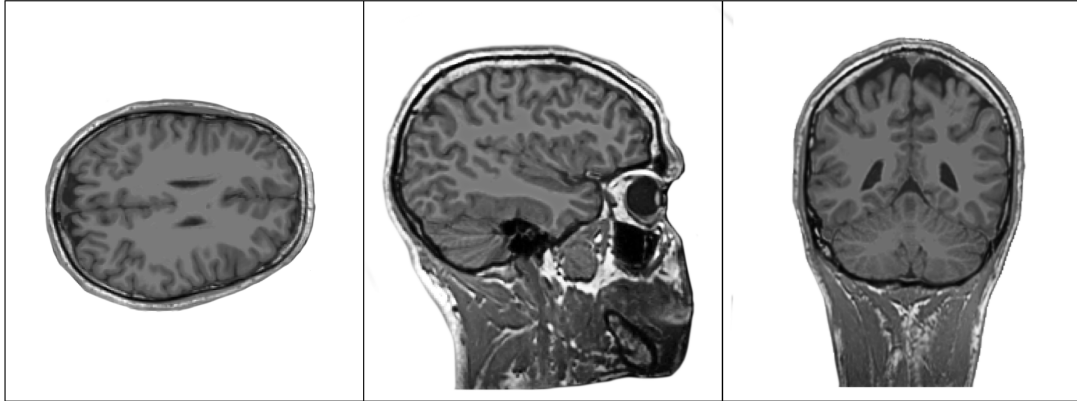


Figure 2.4: MRI scan cross sections of a human head, from left to right in z , y and x direction. The grayscale show the different tissue types. Well visible the cortex, consisting of grey matter, surrounding the white matter. The data set was provided by the Neuroimaging Center Dresden.

spin-spin interactions. Now to distinguish tissues the relaxation times T1 or T2 are taken, because the different time spans correspond to a specific type of tissue. Table 2.1 shows three relevant relaxation times for tissue in the brain. Depending on which time is measured in a MRI scan, the data are called T1 or T2 weighted. The T1 weighted data is well suited for brain analysis. Figure 2.4 shows the final output of a T1 weighted image set, where the structure of the brain tissue and the surrounding skull is already identifiable. Used for the data acquisition was a 3T-MRI-system from Siemens located at Neuroimaging Center Dresden, the performed scan was T1 weighted.

2.2.2 EEG: Electric Brain Activity Measurement

EEG is one of the most used and well known clinical diagnostic methods. It measures the electric potential which is produced by electrophysiological processes in the human body, e.g. in the heart or the brain, by attaching electrodes onto the skin.

The electrodes' positions are ordered relative to anatomical fix points. These are the nasion, which denotes the junction from nose and forehead, and the inion, which corresponds to the peak at the back of the head, see Figure 2.5. At these positions a voltage is received and registered over time.

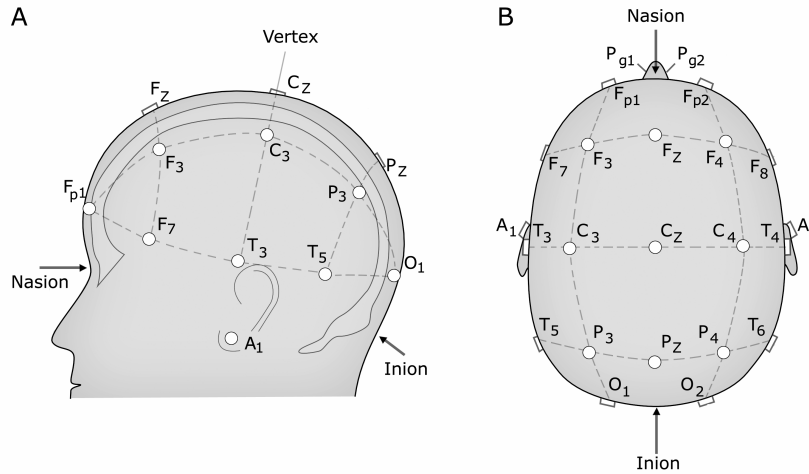


Figure 2.5: Schematic view on the electrode positions in an EEG experiment. Inion, Nasion and Vertex are reference points to describe the orientation of the head. [15]

An advantage of EEG is the high time resolution of the data, because the EEG pattern reacts very quickly to activity changes inside the body. The downside, however, exists in terms of the unknown origin of the source and therefore the necessary source localization, a task which remains challenging to deliver accurate results. In comparison MRI can also be used to measure brain activity, this method is then called functional MRI (fMRI). While this approach directly provides the location information of the active regions, it lacks a high time resolution. This is due to the underlying physiological process used in fMRI to determine active regions in the brain, the change of oxygen concentration. Its time delay is much higher than the electromagnetic processes at synapses, measured in EEG.

Advantage of MRI-EEG Correlation Experiments For this reason scientists tried to combine the advantages of MRI and EEG to overcome their individual limitations. A MRI-EEG correlation experiment provides both, a MRI scan, where the exact positions of the electrodes are included and from which a realistic head model can be constructed, and an EEG data set of the same proband. If an already known stimulus, whose source position is already established, is measured in the EEG, this data can function as reference values at the electrode positions for any computer simulation. This offers a huge opportunity for verification of the forward model in realistic head geometries, since there are no analytic solutions for complex geometries.

2.3 Discretization and Operator Approximation by Particles

The widely used concepts for implementing a simulation of the *forward problem* are meshbased methods, like Finite Element Methods (FEM) or Boundary Element Methods (BEM). Also in recent research more attention has been paid to the utilization of realistic head models instead of standardized or even spherical head models. This, however, leaves the usually used meshbased approaches as a very computationally expensive tool. Therefore recent work tries to use meshless methods, for their advantageous performance in complex geometries. Here the work of Ellenrieder et al. [16] and Ala et al. [17] should be given for an example.

In particle methods the computational elements are called particles and carry three properties, the position \mathbf{x}_p , their respective volumes V_p and one called weights (or strengths) ω_p . They don't have to relate to physical equivalents like molecules or atoms, but nevertheless they can also be used as data abstraction. Particle methods are well known from smoothed particle hydrodynamics and vortex methods.

2.3.1 Continuum Particle Methods

In continuum particle methods the approximation of smooth functions $f(x) : \mathbb{R}^n \rightarrow \mathbb{R}$ is done by discretizing integrals over a set of scattered particles. This can be outlined in three steps.

Convolution with δ In the first step the convolution with the delta distribution is used to represent f as an integral for any \mathbf{x}

$$f(\mathbf{x}) = (f * \delta)(\mathbf{x}) = \int f(\mathbf{y})\delta(\mathbf{y} - \mathbf{x})d\mathbf{y}.$$

Although an elegant way, the delta distribution possesses a problem—it is irregular and hence the discretization of the integral needs further considerations. It can, however, be solved with the aid of regularization.

Regularization of δ The main idea therefore is to replace the irregular delta distribution δ with a kernel function ξ_ε , with characteristic kernel width ε , such that ξ_ε converges to δ for ε tending to zero $\lim_{\varepsilon \rightarrow 0} \xi_\varepsilon$. ξ_ε is often referred to as kernel, smoothing kernel or weight function. Here, it will be consistently called kernel.

$$f(\mathbf{x}) = \int f(\mathbf{y})\xi_\varepsilon(\mathbf{y} - \mathbf{x})d\mathbf{y}$$

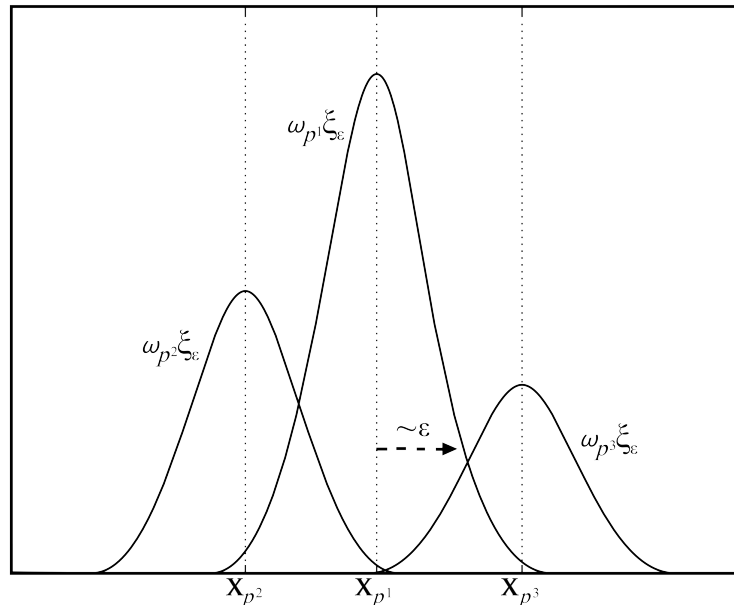


Figure 2.6: Three particles with a Gaussian mollification kernel possessing different weights w_{p^i} . [19]

Also it has to fulfill the same restrictions as the delta distribution, i.e. its support needs to be compact¹ and it has to be normalized.

$$\int \xi_\varepsilon(\mathbf{x}) d\mathbf{x} = 1. \quad (2.8)$$

Usually, because of Eq. 2.8, additionally a scaling condition is required for $\xi_\varepsilon(\mathbf{z}) = \varepsilon^{-n} \xi(\mathbf{z}/\varepsilon)$. This constraint has the benefit of allowing epsilon to change without violating 2.8. Since ξ_ε is an approximation of δ , it is containing an error, the mollification error. To ensure an accuracy of order r , the first $r - 1$ moment conditions of δ have to be conserved. The r -th moment is defined as

$$\int \mathbf{x}^r \xi_\varepsilon(\mathbf{x}) d\mathbf{x} \quad (2.9)$$

and thus for the conversion to remain valid

$$\int \mathbf{x}^r \xi_\varepsilon(\mathbf{x}) d\mathbf{x} = \int x^r \delta(\mathbf{x}) d\mathbf{x} \quad (2.10)$$

For a kernel of order r the mollification error is of order

$$f_\varepsilon = f + O(\varepsilon^r). \quad (2.11)$$

Discretization over particles Finally the integral can be discretized by mid-point quadrature over scattered particle positions. Therefore the integral $\int f d\mathbf{y}$ is

¹The compact support for the kernel is reasoned by Degond et al.[18].

replaced with a sum over the particles at position \mathbf{x}_p

$$f(\mathbf{x}_q) = \sum_p v_p \cdot f(x_p). \quad (2.12)$$

Here the second error occurs due to this discretization and is of order $(\frac{h}{\epsilon})$, with h denoting the interparticle spacing. The total error made is thus

$$f_\epsilon^h = f + O(\epsilon^r) + O\left(\frac{h}{\epsilon}\right). \quad (2.13)$$

2.3.2 Operator Approximation: the Method of Particle Strength Exchange

From here on out, to retain clarity of the formulas, a multi-index notation is used and defined as followed.

Multi-index Notation A multi-index $\boldsymbol{\alpha} = (\alpha_1, \dots, \alpha_n) \in \mathbb{N}^n$ is a n -tuple of natural non-negative numbers and will be denoted by the Greece letters $\boldsymbol{\alpha}$, $\boldsymbol{\beta}$ or $\boldsymbol{\gamma}$. The absolute and factorial are

$$|\boldsymbol{\alpha}| = \sum_{i=1}^n \alpha_i, \quad \boldsymbol{\alpha}! = \prod_{i=1}^n \alpha_i.$$

Furthermore the potency definition with a vector $\mathbf{x} = (x_1, \dots, x_n)^T \in \mathbb{R}^n$ is

$$\mathbf{x}^\alpha = \prod_{i=1}^n x_i^{\alpha_i}.$$

Derivatives of functions with several variables $f(\mathbf{x}) : \mathbb{R}^n \rightarrow \mathbb{R}$ are written as

$$D^\beta f(\mathbf{x}) = \frac{\partial^{|\beta|} f(\mathbf{x})}{\partial x_1^{\beta_1} \partial x_2^{\beta_2} \dots \partial x_n^{\beta_n}}.$$

An important aspect to line out is how to read expressions of the form $|\boldsymbol{\alpha}| = k$, $k \in \mathbb{N}_0$. Here the set of α contains not only all the possible tuples of α to construct the sum with, they also consider their permutations, e.g. if $\boldsymbol{\alpha} \in \mathbb{N}^2$ and $k = 3$, the resulting tuples are $\boldsymbol{\alpha}_1 = (3, 0)$, $\boldsymbol{\alpha}_2 = (2, 1)$ and their permutations $\boldsymbol{\alpha}_3 = (0, 3)$, $\boldsymbol{\alpha}_4 = (1, 2)$.

General PSE Operators The method of Particle Strength Exchange (PSE) follows the idea of using kernels to consistently approximate differential operators and moreover guarantees the conservation of particle strength in particle-particle interactions. It was first introduced in 1989 by Degond and Mas-Gallic ([18]) for

diffusion and convection-diffusion problems and upon this groundwork Eldredge et al. [20] developed a framework for arbitrary derivatives. In general a PSE-operator for approximating the action of $D^\beta f(\mathbf{x}) = Qf(\mathbf{x}) =$ has the form

$$Q^\beta f(\mathbf{x}) = \frac{1}{\varepsilon^{|\beta|}} \int (f(\mathbf{y}) \mp f(\mathbf{x})) \eta_\varepsilon^\beta(\mathbf{x} - \mathbf{y}) d\mathbf{y}, \quad (2.14)$$

where the minus is chosen when $|\beta|$ is even and positive when $|\beta|$ is odd. The difficulty in this integral representation is however to find a kernel $\eta_\varepsilon^\beta(\mathbf{x})$, which approximates D^β . Although $\eta_\varepsilon^\beta(\mathbf{x})$ has not necessarily to be the same as $\xi_\varepsilon(\mathbf{x})$, its characteristic $\eta_\varepsilon^\beta(\mathbf{z}) = \varepsilon^{-n} \eta^\beta(\frac{\mathbf{z}}{\varepsilon})$ is demanded, too.

Integral Approximation Now to determine kernels for arbitrary derivatives, the idea from [20] is followed, starting with the Taylor series of a function f at \mathbf{y}

$$f(\mathbf{y}) = f(\mathbf{x}) + \sum_{|\alpha|=1}^{\infty} (\mathbf{y} - \mathbf{x})^\alpha D^\alpha f(\mathbf{x}). \quad (2.15)$$

The next step is to subtract or add $f(\mathbf{x})$, depending on $|\beta|$ being odd or even, on both sides and convolute the equation with the unknown kernel $\eta_\varepsilon^\beta(\mathbf{x})$. This leads with consideration of Eq. 2.14 to

$$Q^\beta f(\mathbf{x}) = \frac{1}{\varepsilon^\beta} \sum_{|\alpha|=1}^{\infty} D^\alpha f(\mathbf{x}) \int (\mathbf{y} - \mathbf{x})^\alpha \eta_\varepsilon^\beta(\mathbf{x} - \mathbf{y}) d\mathbf{y} + f_0, \quad (2.16)$$

with

$$f_0 = \begin{cases} 0, & |\beta| \text{ even,} \\ 2 \varepsilon^{-\beta} \int f(\mathbf{x}) \eta_\varepsilon^\beta(\mathbf{x} - \mathbf{y}) d\mathbf{y}, & |\beta| \text{ odd.} \end{cases}$$

At this point the continuous α -moments

$$M_\alpha = \int (\mathbf{x} - \mathbf{y})^\alpha \eta^\beta(\mathbf{x} - \mathbf{y}) d\mathbf{y} = \int \left(\frac{\mathbf{z}}{\varepsilon}\right)^\alpha \eta_\varepsilon^\beta(\mathbf{z}) d\mathbf{y} \quad (2.17)$$

are introduced. Note that here the characteristic of the kernel $\eta_\varepsilon^\beta(\mathbf{z}) = \varepsilon^{-n} \eta^\beta(\frac{\mathbf{z}}{\varepsilon})$ is already exploited. Then isolation of the derivative(s)² D^β on the right hand side results in

$$Q^\beta f(\mathbf{x}) = \frac{(-1)^{|\beta|}}{\beta!} M_\beta D^\beta f(\mathbf{x}) + \sum_{\substack{|\alpha|=1 \\ \alpha \neq \beta}}^{\infty} \frac{(-1)^{|\alpha|}}{\alpha!} \varepsilon^{|\alpha|-|\beta|} M_\alpha D^\alpha f(\mathbf{x}) \quad (2.18)$$

²Also linear combinations of derivatives can be approximated.

Finally, to approximate $Q^\beta f(\mathbf{x})$ with order of accuracy r , the set of conditions

$$M_\alpha = \begin{cases} (-1)^{|\beta|} \beta!, & \alpha = \beta, \\ 0, & \alpha \neq \beta, \end{cases} \quad 1 \leq |\alpha| \leq |\beta| + r - 1, \quad (2.19)$$

for the moments M_α are imposed and in addition

$$\int \left| \left(\frac{\mathbf{z}}{\varepsilon} \right)^\alpha \eta_\varepsilon^\beta(\mathbf{z}) \right| d\mathbf{z} < \infty, \quad |\alpha| = |\beta| + r$$

is demanded. Under these terms the mollification error $\epsilon_\varepsilon(\mathbf{x}) = Qf(\mathbf{x}) - Q^\beta f(\mathbf{x})$ can be bounded as

$$|\epsilon_\varepsilon(\mathbf{x})| \leq C\varepsilon^r,$$

with some constant³ C . Considering a template for $\eta_\varepsilon^\beta(\mathbf{x})$ and the set of moment conditions 2.19, it is now possible to construct a kernel which satisfies them and, hence approximates Q^β . For examples on how to do this, see [20].

Discretization Once a kernel is determined the last step is to discretize the operator, defined in Eq. 2.14, by midpoint quadrature over particles

$$Q_h^\beta f(\mathbf{x}) = \frac{1}{\varepsilon^{|\beta|}} \sum_{p \in N(\mathbf{x})} v_p (f(\mathbf{x}_p) \mp f(\mathbf{x})) \eta_\varepsilon^\beta(\mathbf{x} - \mathbf{x}_p).$$

Here $N(\mathbf{x})$ is the amount of all particles in a neighbourhood around \mathbf{x} and usually defined by a cutoff radius r_c . In turn, the cutoff radius is mostly chosen such that $N(\mathbf{x})$ coincides on a certain level of accuracy with the kernel support. The discretization error $\epsilon_h(\mathbf{x}) = Qf(\mathbf{x}) - Q_h^\beta f(\mathbf{x})$ is bounded as

$$|\epsilon_h(\mathbf{x})| \leq C \frac{h^m}{\varepsilon^{m+1}}. \quad (2.20)$$

2.3.3 The Discretization Corrected PSE Operators

The Discretization Corrected PSE (DCPSE) Operator, introduced by Schrader et al [21], focuses on removing the discretization error 2.20 from the PSE operator approximation. Instead of deriving the Taylor series with the integral approximation, it considers the already discretized approximation and thus the overall error $\epsilon(\mathbf{x}) = \epsilon_h(\mathbf{x}) + \epsilon_\varepsilon(\mathbf{x})$. Therefore Eq. 2.18 writes

$$Q_h^\beta f(\mathbf{x}) = \frac{(-1)^{|\beta|}}{\beta!} Z_h^\beta D^\beta f(\mathbf{x}) + \sum_{\substack{|\alpha|=1 \\ \alpha \neq \beta}}^{\infty} \frac{(-1)^{|\alpha|}}{\alpha!} \varepsilon^{|\alpha|-|\beta|} Z_h^\alpha D^\alpha f(\mathbf{x}) \quad (2.21)$$

³For further details on C , see [18].

with

$$f_0 = \begin{cases} 0, & |\beta| \text{ even,} \\ 2\varepsilon^{-|\beta|} Z_h^0 f(\mathbf{x}), & |\beta| \text{ odd.} \end{cases}$$

and the corresponding discrete moments Z_h^α in n dimensions

$$Z_h^\alpha = \frac{1}{\varepsilon^n} \sum_{p \in N(\mathbf{x})} v_p \left(\frac{\mathbf{x} - \mathbf{x}_p}{\varepsilon} \right)^\alpha \eta_\varepsilon^\beta \left(\frac{\mathbf{x} - \mathbf{x}_p}{\varepsilon} \right).$$

Also the set of moment conditions has to be adjusted and now looks for all $|\beta| \neq 0$

$$Z_h^\alpha = \begin{cases} (-1)^{|\beta|} \beta!, & \alpha = \beta, \\ 0, & \alpha \neq \beta, \quad \alpha_{min} \leq |\alpha| \leq |\beta| + r - 1, \\ < \infty, & |\alpha| = |\beta|, \end{cases} \quad (2.22)$$

for $|\beta| = 0$, however, it is

$$Z_h^\alpha = \begin{cases} \frac{1}{2}, & \alpha = 0, \\ 0, & \alpha \neq 0, \quad 1 \leq |\alpha| \leq r - 1, \\ < \infty, & |\alpha| = 0. \end{cases} \quad (2.23)$$

For the kernel η_ε^β the template

$$\eta_\varepsilon^\beta(\mathbf{x}, \mathbf{z}) = \left(\sum_{|\gamma|=\alpha_{min}}^{|\beta|+r-1} a_\gamma(\mathbf{x}) \mathbf{z}^\gamma \right) e^{-|\mathbf{z}|^2} = C(\mathbf{x}, \mathbf{z}) \Theta(\mathbf{z}), \quad \mathbf{z} = \frac{\mathbf{x} - \mathbf{x}_p}{\varepsilon}, \quad (2.24)$$

is chosen. It consists of a polynomial correction function $C(\mathbf{x}, \mathbf{z})$ and the so called window function $\Theta(\mathbf{z})$. For further details on what possible choices there are, see [22]. To determine the unknown coefficients $a_\gamma(\mathbf{x})$, Eq. 2.24 is put into Eq. 2.25 and the following linear system of equations is obtained

$$\sum_{|\gamma|=\alpha_{min}}^{|\beta|+r-1} a_\gamma(\mathbf{x}) w_\alpha^\gamma(\mathbf{x}) = \begin{cases} (-1)^{|\beta|} \beta!, & \alpha = \beta, \\ 0, & \alpha \neq \beta, \end{cases} \quad \forall \alpha_{min} \leq |\alpha| \leq |\beta| + r - 1, \quad (2.25)$$

with weights

$$w_\alpha^\gamma(\mathbf{x}) = \frac{1}{\varepsilon^{|\alpha+\gamma|+n}} \sum_{p \in N(\mathbf{x})} v_p (\mathbf{x} - \mathbf{x}_p)^{\alpha+\gamma} e^{-|\frac{\mathbf{x}-\mathbf{x}_p}{\varepsilon}|^2}.$$

In this linear system of equations the multi-index γ indicates the columns and therefore the unknown coefficients a_γ , whereas α indexes the rows or the number of equations. The count of columns and rows is equal and can be expressed with

m

$$m = \binom{|\beta| + r - 1 + n}{n} - \alpha_{\min}. \quad (2.26)$$

In the end the DCPSE Operator is

$$Q_h^\beta f(\mathbf{x}) = \frac{1}{\varepsilon^{|\beta|}} \sum_{p \in N(\mathbf{x})} v_p (f(\mathbf{x}_p) \mp f(\mathbf{x})) \eta_\varepsilon^\beta(\mathbf{x} - \mathbf{x}_p),$$

and in the strong formulation, i.e. setting the particle volumes to one, it is

$$Q_h^\beta f(\mathbf{x}) = \frac{1}{\varepsilon^{|\beta|}} \sum_{p \in N(\mathbf{x})} (f(\mathbf{x}_p) \mp f(\mathbf{x})) \eta_\varepsilon^\beta(\mathbf{x} - \mathbf{x}_p). \quad (2.27)$$

From here on out the DCPSE operator is considered in its strong form.

Chapter 3

Development of the Forward Model Framework

3.1 DCPSE Operator: Construction and Characteristics

A closer look is now paid to the construction of a DCPSE Operator. While the one dimensional case is straight forward, the two dimensional case gets more complicated, but the transition to any more dimensions will then be trivial. To cover the complexity of the multi-index notation, while keeping the clarity of the construction, a two-dimensional DCPSE Operator with order of accuracy $r = 2$ is chosen for a design study. Afterwards the influence of parameters of choice upon the operator performance and accuracy will be discussed.

3.1.1 Exemplary Construction of a DCPSE Operator

Consider the second partial differential operator for the function $f : \mathbb{R}^2 \rightarrow \mathbb{R}$ with respect to the variable x

$$D^{(2,0)} f(x, y) = \frac{\partial^2 f(x, y)}{\partial^2 x}.$$

In two dimensions β is a pair of non-negative integers, here $\beta = (2, 0)$. To construct the polynomial correction function up to the order of r , its monomial base has to be determined, i.e. \mathbf{x}^γ in Eq. 2.24, with the coefficients a_γ .

Monomial Base It is defined by the order of accuracy r , the dimension $n = 2$ and finally the structure of the differential operator $D^{(2,0)}$ itself. Since $|\beta| = 2$, α_{min} equals 1 and the number of monomials m is 9. The sum in Eq. 2.24 goes

from $|\gamma| = 1$ to $|\gamma| = 3$ and all possible γ , nine in number, are

$$\begin{aligned} & (1, 0), \quad (0, 1), \\ & (2, 0), \quad (1, 1), \quad (0, 2), \\ & (3, 0), \quad (2, 1), \quad (1, 2), \quad (0, 3). \end{aligned}$$

The weights w_α^γ are obtained in the same way. Because there are nine monomials, the number of weights is 81 or let W be the matrix of weights, it is a 9×9 matrix,

$$W = \begin{pmatrix} w_{(1,0)}^{(1,0)} & w_{(1,0)}^{(0,1)} & \cdots & w_{(1,0)}^{(0,3)} \\ w_{(0,1)}^{(1,0)} & w_{(0,1)}^{(0,1)} & \cdots & w_{(0,1)}^{(0,3)} \\ \vdots & \vdots & \ddots & \vdots \\ w_{(0,3)}^{(1,0)} & w_{(0,3)}^{(0,1)} & \cdots & w_{(0,3)}^{(0,3)} \end{pmatrix}.$$

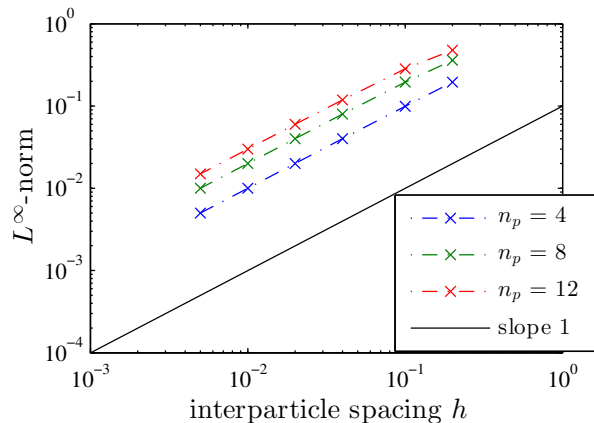
From here the linear system of equations 2.25 has to be solved and the calculated coefficients a_γ are inserted in the DCPSE-template 2.24. Also in Eq. 2.27 the minus sign is chosen.

In MATLAB the values are stored as a sparse matrix in such a way that in each row the values for one particle are saved and matrix multiplication yields the sum in Eq. 2.27. Since only the neighbouring particles are considered, the entries for all non-neighbouring particles are set to zero. This enables the full utilization of MATLAB's fast matrix operations, while limiting excessive need of memory, because for a sparse matrix only the non-zero elements and their matrix indices are physically saved.

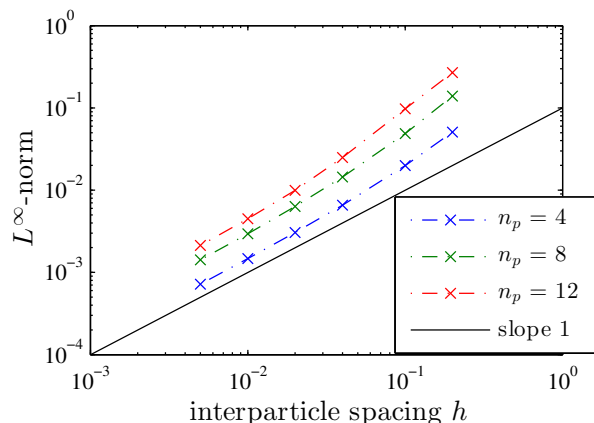
3.1.2 Parameters of Choice and Operator Convergence

The parameters of choice for the DCPSE operator are the kernel width ε , the cutoff radius r_c and the order of accuracy r . They have a high impact on the operator performance and accuracy. A brief summary of the most important characteristics is given now. For a very detailed discussion from a mathematical as well as from a numerical point of view see Schrader [22].

Cutoff Radius r_c The cutoff radius r_c has an influence on both the accuracy and the performance. Recall formula 2.25 for the system of equations and Eq. 2.26



(a)



(b)

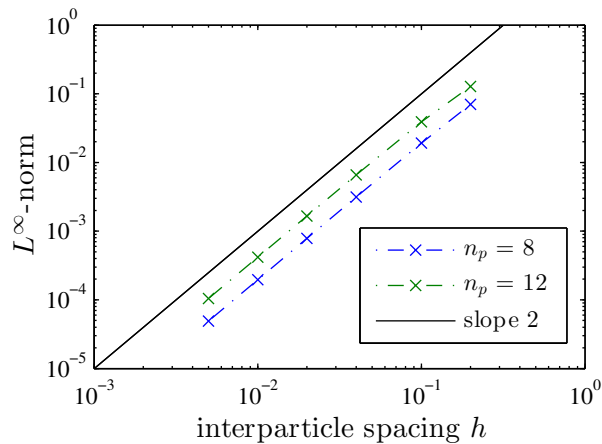
Figure 3.1: L^∞ norm for the one-dimensional first and second derivative of a trigonometric test function for a first derivative (a) and second derivative (b) DCPSE approximation with $r = 1$, $c = 1$, and n_p neighbouring particles inside the cutoff range r_c

for the number of both rows and columns. To guarantee that the system does not break down, the number of neighbouring particles may not be less than m , the number of unknowns.

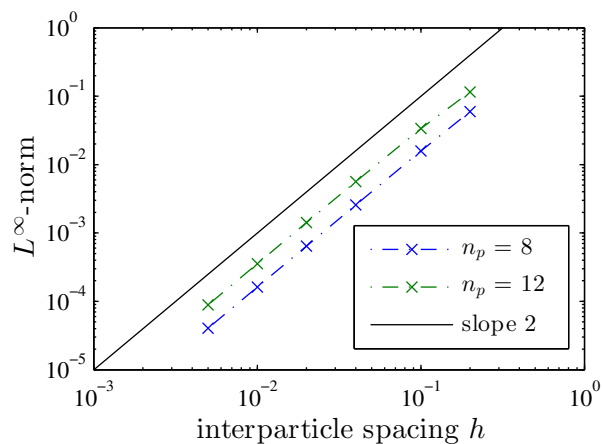
Any additional particle will not only increase the computational cost, moreover it will influence the accuracy negatively [22].

Kernel Width ε A key parameter for the operator stability is ε . It has to be coupled to the average interparticle spacing h via the ratio $c = \frac{h}{\varepsilon}$. However for smaller c the accuracy of the operator is expected to be decreased [22]. An explanation is the less peaked window function, which results in more smoothing overall.

Order of Accuracy r The parameter r , which defines the order of the correction polynomial, will improve the accuracy when increased, while also scaling up the



(a)



(b)

Figure 3.2: L^∞ norm for the one-dimensional first (a) and second derivative of a trigonometric test function for a DCPSE operator with $r = 2$, $c = 1$, and n_p neighbouring particles inside the cutoff range r_c

computational cost. This is due to the additional number of unknown parameters a_γ and the enlarged linear system of equations to solve.

Error Measures For the error measure the L^2 -norm

$$L^2 = \frac{1}{N_p} \left(\sum_{p=1}^{N_p} (D^\beta f(\mathbf{x}_p) - Q_h^\beta f(\mathbf{x}_p))^2 \right)^{\frac{1}{2}}$$

and the L^∞ -norm

$$L^\infty = \sup_{p \in N_p} |D^\beta f(\mathbf{x}_p) - Q_h^\beta f(\mathbf{x}_p)|$$

are used. Here N_p denotes the total number of particles with respective position \mathbf{x}_p , while the term $D^\beta f(\mathbf{x}_p) - Q_h^\beta f(\mathbf{x}_p)$ expresses the error between the analytical and the numerical value. in Figure 3.1 and Figure 3.2 convergence plots for a fixed ratio $c = 1$ are shown, but different cutoff radii r_c . Notice that for an increasing number

of neighbouring particles the accuracy of the approximation decreases slightly. Also for a higher order of accuracy r the obtained accuracy is increased. Since the L^2 norm and the L^∞ norm delivered the same convergence characteristics, only the L^∞ is represented.

3.2 Utilization of the DCPSE Operator for Solving Linear Partial Differential Equations

The DCPSE Operator can also be used to solve linear inhomogeneous PDEs, e.g of the form

$$\sigma(\mathbf{x})D^\beta f(\mathbf{x}) = g(\mathbf{x}),$$

with Neuman or Dirichlet boundary conditions. Here $\sigma(\mathbf{x})$ is not necessarily a constant coefficient, but a scalar field depending on $\mathbf{x} = (x_1, x_2, \dots, x_n)$ and $g(\mathbf{x})$, also a scalar field, is a given inhomogeneity. Of course linear combinations of differential operators D^β are possible. Therefore the operator was put inside a framework which is able to provide a solution of the PDE with respect to the boundary conditions. How the DCPSE Operator fits into this framework and how the boundary conditions are inserted will be discussed now.

3.2.1 Associated Shape Functions

Since the DCPSE Operator Q^β is based on the difference or sum of functions at point \mathbf{x} , it can be formulated in a way that matrix multiplication with the function values at the particle positions gives directly the result $Q^\beta f(\mathbf{x}_q) = (\underline{A}^\beta f)(\mathbf{x}_q)$ that is approximated. This matrix \underline{A}^β will be called the associated shape function from here on out. For the construction, recall the DCPSE formula for particle q

$$Q_h^\beta f(\mathbf{x}_p) = \sum_{p \in N(\mathbf{x}_q)} (f(\mathbf{x}_p) \mp f(\mathbf{x}_q)) \eta_{qp}^\beta.$$

With rearrangement one obtains

$$Q_h^\beta f(\mathbf{x}_p) = \frac{1}{\varepsilon^{|\beta|}} \sum_{p \in N(\mathbf{x}_q)} f(\mathbf{x}_p) \eta_{qp}^\beta \mp \sum_{p \in N(\mathbf{x}_q)} f(\mathbf{x}_q) \eta_{qp}^\beta,$$

which can be written in matrix notation as $\underline{A}^\beta \cdot \mathbf{f}$, where

$$\underline{A}^\beta = \begin{pmatrix} \mp(\eta_{11}^\beta + \eta_{12}^\beta + \dots) & \eta_{12}^\beta & \cdots & 0 \\ \eta_{21}^\beta & \mp(\eta_{21}^\beta + \eta_{22}^\beta + \dots) & \cdots & 0 \\ \vdots & \vdots & \ddots & \vdots \\ 0 & 0 & \cdots & \mp(\eta_{N_p,1}^\beta + \eta_{N_p,2}^\beta + \dots) \end{pmatrix}$$

and

$$\mathbf{f} = \begin{pmatrix} f(\mathbf{x}_1) \\ f(\mathbf{x}_2) \\ \vdots \\ f(\mathbf{x}_{N_p}) \end{pmatrix}.$$

Note that for reasons of clarity, the matrix notation of \underline{A}^β is simplified since a diagonal sparse matrix is assumed. In general the matrix \underline{A}^β does not possess this characteristic, but in that case nothing changes except the position of the non-zero elements. In matrix notation the expression for an approximated differential operator Q^β at all particle positions \mathbf{x}_q is then

$$\begin{pmatrix} Q^\beta f(\mathbf{x}_1) \\ Q^\beta f(\mathbf{x}_2) \\ \vdots \\ Q^\beta f(\mathbf{x}_{N_p}) \end{pmatrix} = \begin{pmatrix} A_{11}^\beta & A_{12}^\beta & \cdots & 0 \\ A_{21}^\beta & A_{22}^\beta & \cdots & 0 \\ \vdots & \vdots & \ddots & \vdots \\ 0 & 0 & \cdots & A_{N_p, N_p}^\beta \end{pmatrix} \cdot \begin{pmatrix} f(\mathbf{x}_1) \\ f(\mathbf{x}_2) \\ \vdots \\ f(\mathbf{x}_{N_p}) \end{pmatrix}.$$

3.2.2 Formulation of Partial Differential Equations with Associated Shape Functions

To solve a PDE, an approach based on creating and solving a linear system of equations of the form $\underline{A}\mathbf{f} = \mathbf{b}$ was used. Here \underline{A} denotes the coefficient matrix, \mathbf{f} is the vector of unknowns and \mathbf{b} the solution vector. This method contains two major steps, first creating the linear system of equations, for which then a numerical solver can be used, and then inserting the boundary conditions in this LSE. Consider a linear PDE for the unknown scalar function $f(\mathbf{x}) : \mathbb{R}^n \rightarrow \mathbb{R}$ in a n -dimensional domain Ω , with a boundary $\partial\Omega$,

$$(\sigma_1(\mathbf{x})D^{\beta_1} + \sigma_2(\mathbf{x})D^{\beta_2}) f(\mathbf{x}) = g(\mathbf{x})$$

and homogeneous Neuman,

$$\frac{\partial f(\mathbf{x})}{\partial \mathbf{n}} = \nabla f(\mathbf{x}) \cdot \mathbf{n}(\mathbf{x}) = 0 \quad \mathbf{x} \in \partial\Omega, \quad (3.1)$$

or homogeneous Dirichlet boundary conditions,

$$f(\mathbf{x}) = 0 \quad \mathbf{x} \in \partial\Omega. \quad (3.2)$$

Here \mathbf{n} is the outer-pointing normal of $\partial\Omega$ and the count of differential operators D^{β_i} is restricted to two, generalization to an arbitrary number, however, is easily possible.

Construction of the LSE For each D^{β_i} the associated shape function of the DCPSE approximation Q^{β_i} is \underline{A}^{β_i} , a $N_p \times N_p$ matrix. There every row q , representing the q -th particle, has to be multiplied with the corresponding coefficient $\sigma_i(\mathbf{x}_q)$. In MATLAB it is desirable for performance reasons to formulate this in matrix notation.

It is possible to represent the coefficients $\sigma_i(\mathbf{x})$ with diagonal matrices. The vector elements of the coefficient values at each particle position, $\boldsymbol{\sigma}_i = (\sigma_i(\mathbf{x}_1), \dots, \sigma_i(\mathbf{x}_{N_p}))^T$, are the diagonal entries and matrix multiplication with \underline{A}^{β_i} yields the desired result. This is due to the characteristic result of the multiplication of a diagonal $k \times k$ matrix \underline{d} with an arbitrary $k \times k$ matrix \underline{M} , which is

$$\begin{pmatrix} d_1 & 0 & \cdots & 0 \\ 0 & d_2 & \ddots & \vdots \\ \vdots & \ddots & \ddots & 0 \\ 0 & \cdots & 0 & d_k \end{pmatrix} \cdot \begin{pmatrix} M_{11} & M_{12} & \cdots & M_{1k} \\ M_{21} & M_{22} & \cdots & M_{2k} \\ \vdots & \vdots & \ddots & \vdots \\ M_{k1} & M_{k2} & \cdots & M_{kk} \end{pmatrix} = \begin{pmatrix} d_1 M_{11} & d_1 M_{12} & \cdots & d_1 M_{1k} \\ d_2 M_{21} & d_2 M_{22} & \cdots & d_2 M_{2k} \\ \vdots & \vdots & \ddots & \vdots \\ d_k M_{k1} & d_k M_{k2} & \cdots & d_k M_{kk} \end{pmatrix}.$$

In the end this leads to the following expression for the PDE

$$\left(\text{diag}(\boldsymbol{\sigma}_1) \cdot \underline{A}^{\beta_1} + \text{diag}(\boldsymbol{\sigma}_2) \cdot \underline{A}^{\beta_2} \right) \mathbf{f} = \mathbf{g}, \quad (3.3)$$

with $\boldsymbol{\sigma}_i = (\sigma_i(\mathbf{x}_1), \dots, \sigma_i(\mathbf{x}_{N_p}))^T$ and $\mathbf{f} = (f(\mathbf{x}_1), \dots, f(\mathbf{x}_{N_p}))^T$. Now Eq. 3.3 is of the form $\underline{A}\mathbf{f} = \mathbf{g}$, because every matrix on the left hand side (LHS) is known, and can be numerically solved. Note, that the same letter f symbolizes the vector \mathbf{f} and the function f to show the relationship between both.

Implementation of Boundary Conditions Starting from Eq. 3.3, assume that the LSE is of the form $\underline{A}\mathbf{f} = \mathbf{b}$ and that the position of the boundaries is well known, so particles can easily be placed there. Inserting the boundary conditions is then done by updating the boundary particles in the LSE for the PDE. This means that each updated row, corresponding to a boundary particle, has to express Eq. 3.1 or Eq. 3.2 with respect to the boundary condition. The case of Dirichlet boundary conditions is rather simple, one has to update the q -th

row, which represents particle q on a boundary with Dirichlet boundary condition, only with zeros, except at the column index q to 1. In other terms the updated row is the q -th row of a $N_p \times N_p$ identity matrix. Also the q -th element of the solution vector has to be changed accordingly, to $g(\mathbf{x}_q)$.

$$\begin{pmatrix} \vdots & & \\ A_{q1} & \cdots & A_{qN_p} \\ \vdots & & \end{pmatrix} \rightarrow \begin{pmatrix} \vdots & & & & \\ 0 & \cdots & 0 & 1_{qq} & 0 & \cdots & 0 \\ \vdots & & & & & & \end{pmatrix}$$

For Neuman boundary conditions, the replacement is more complex but the concept remains the same. The goal is again to change the corresponding row of the boundary particle entries which express the condition equation. Therefore recall Eq. 3.1 with the summation over the dimensions not the particles

$$\nabla f(\mathbf{x}) \cdot \mathbf{n}(\mathbf{x}) = \sum_{i=1}^n \frac{\partial f(x_i)}{\partial x_i} n_{x_i} = 0, \quad \mathbf{x} \in \partial\Omega.$$

Exemplary, the concept to change the q -th row for one summand will be shown in two dimensions. If one considers the DCPSE approximation for $\frac{\partial}{\partial x}$ to be $Q^{(1,0)}$ and $\frac{\partial}{\partial y}$ to be $Q^{(0,1)}$, the associated shape functions will be $\underline{A}^{(1,0)}$ and $\underline{A}^{(0,1)}$. For the construction of the new row, the q -th rows of $\underline{A}^{(1,0)}$ and $\underline{A}^{(0,1)}$ are multiplied with n_x and n_y respectively. The q -th row of the coefficient matrix changes to

$$\begin{pmatrix} \vdots & & \\ A_{q1} & \cdots & A_{qN_p} \\ \vdots & & \end{pmatrix} \rightarrow \begin{pmatrix} \vdots & & & & \\ n_x A_q^{(1,0)} + n_y A_q^{(0,1)} & \cdots & n_x A_{qN_p}^{(1,0)} + n_y A_{qN_p}^{(0,1)} \\ \vdots & & & & \end{pmatrix}.$$

3.3 Forward Model Framework

3.3.1 Single Region and Multi Region Approach for the Forward Problem

A realistic model of the domain in the electric *forward problem* is often taken to be a domain with distinguished subdomains, where the value of conductivity σ is assumed to be constant. The PDE for the electric potential ϕ can then be written as

$$\nabla \cdot (\sigma(\mathbf{x}) (\nabla \phi(\mathbf{x}))) = -s(\mathbf{x}), \quad \sigma(\mathbf{x}) = \begin{cases} \sigma_i, & \mathbf{x} \in \Omega_i, \\ 0, & \mathbf{x} \notin \Omega, \end{cases} \quad (3.4)$$

additionally considering any existing boundary conditions, Figure 3.3 shows such a domain with three subdomains.

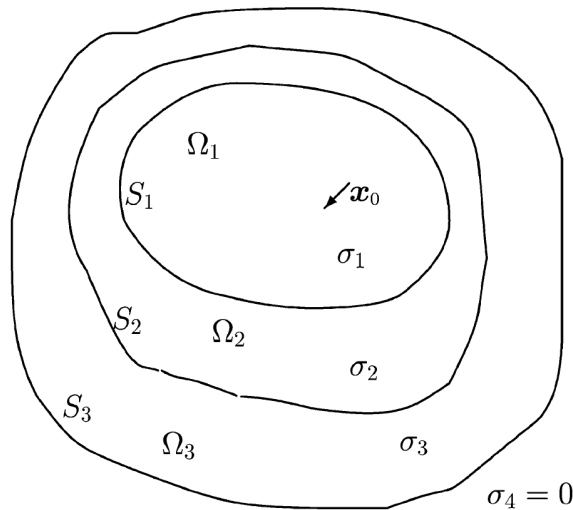


Figure 3.3: Domain Ω with subdomains Ω_i of constant coefficients σ_i . Outside Ω , $\sigma = 0$. The interfaces are denoted with S_i [16]

Single Region For the single region approach the domain is considered as a whole and σ has to be regarded as a discontinuous scalar field and attention has to be paid to the impact of the nabla operator. With the product rule eq. 3.4 becomes

$$(\nabla\sigma(\mathbf{x}))(\nabla\phi(\mathbf{x})) + \sigma(\mathbf{x})(\Delta\phi(\mathbf{x})) = -s(\mathbf{x})$$

The difficulty in this approach is to approximate the derivative of the discontinuous scalar field σ , because at the interfaces the derivative will become infinite, a singularity occurs. It should be pointed out that any approximation attempt without smoothing the discontinuities will be a very poor one by default.

Multi Region The multi region approach aims to avoid this problem and therefore splits Ω in the subdomains Ω_i , where the conductivity value is constant. In that case one ends up with a different PDE for each subdomain and moreover has to require two additional conditions at each interface S_i , the continuity of the electric potential ϕ and the continuity of it's gradient $\nabla\phi$.

$$\begin{aligned}\sigma_i\Delta\phi_i(\mathbf{x}) &= -s(\mathbf{x}), & \mathbf{x} \in \Omega_i \\ \phi_i(\mathbf{x})|_{x \in S_i} &= \phi_{i+1}(\mathbf{x})|_{x \in S_i} \\ \sigma_i\nabla\phi(\mathbf{x})|_{x \in S_i} &= \sigma_{i+1}\nabla\phi(\mathbf{x})|_{x \in S_i}\end{aligned}$$

The second one is often referred to as the continuity of fluxes.

3.3.2 Insertion of a Current Source Dipole

The current source dipole was only considered in the multi region case, it is however equally possible for the single region case. For the multi region approach that leads to the following PDE with interface conditions

$$\begin{aligned}\sigma_i \Delta \phi_i(\mathbf{x}) &= -\mathbf{I}_d \nabla \delta(\mathbf{x} - \mathbf{x}_d), & \mathbf{x} \in \Omega_i \\ \phi_i(\mathbf{x})|_{x \in S_i} &= \phi_{i+1}(\mathbf{x})|_{x \in S_i} \\ \sigma_i \nabla \phi(\mathbf{x})|_{x \in S_i} &= \sigma_{i+1} \nabla \phi(\mathbf{x})|_{x \in S_i}\end{aligned}\tag{3.5}$$

Direct Approach In this approach the source and sink terms are inserted directly at the respective particle positions. This will be called a physical current source dipole. If a sink I_{si} and a source I_{so} , with $I_{so} = -I_{si}$, are inserted at the particle positions q_{so} and q_{si} the q_{so} -th and q_{si} -th entry of the RHS have to be changed to I_{si} and I_{so} .

Subtraction Approach The ideal current source dipole from Eq. 2.7, will be inserted with the subtraction approach as done by [23] and [16]. It considers the solution as superposition of the solutions for an ideal dipole in an infinite homogeneous medium ϕ^∞ and a correction potential ϕ^{cor} ,

$$\phi = \phi^\infty + \phi^{cor}.$$

For ϕ^∞ the solution to the PDE

$$\sigma_0 \Delta \phi^\infty(\mathbf{x}) = -\mathbf{I}_d \nabla \delta(\mathbf{x} - \mathbf{x}_d)\tag{3.6}$$

is well known, see [24], it is

$$\phi^\infty(\mathbf{x}) = \frac{1}{4\pi\sigma_0} \frac{\mathbf{I}_d \cdot (\mathbf{x} - \mathbf{x}_d)}{|\mathbf{x} - \mathbf{x}_d|^3}.$$

And the PDE for the homogeneous medium 3.6 will be subtracted from the actual PDE 3.5 and one obtains the following PDE for ϕ^{cor} ,

$$(\sigma_i - \sigma_0) \Delta \phi^\infty(\mathbf{x}) + \sigma_i \Delta \phi^{cor}(\mathbf{x}) = 0 \quad \mathbf{x} \in \Omega_i.$$

The first term $(\sigma_i - \sigma_0) \Delta \phi^\infty(\mathbf{x})$ is zero at the dipole position, because $\sigma_i = \sigma_0$. For $\mathbf{x} \neq \mathbf{x}_d$, Eq. 3.6 states that $\Delta \phi^\infty(\mathbf{x})$ vanishes everywhere except at the dipole position. Thus, the PDE to solve for ϕ^{cor} is

$$\sigma_i \Delta \phi_i^{cor}(\mathbf{x}) = 0, \quad \mathbf{x} \in \Omega_i,$$

which can be solved numerically. This also leads, with continuity of ϕ_∞ , to changing interface conditions of the form

$$\begin{aligned}\phi_i^{cor}(\mathbf{x})|_{x \in S_i} &= \phi_{i+1}^{cor}(\mathbf{x})|_{x \in S_i}, \\ \sigma_i \nabla \phi^{cor}(\mathbf{x})|_{x \in S_i} - \sigma_{i+1} \nabla \phi^{cor}(\mathbf{x})|_{x \in S_i} &= (\sigma_{i+1} - \sigma_i) \nabla \phi^\infty(\mathbf{x})|_{x \in S_i}.\end{aligned}$$

3.4 Calculating the Electric Potential in Different Geometries

To test and understand the different approaches, the electric potential is calculated in several test geometries. At the start a simple one-dimensional region, where the analytical solution can be calculated, is considered. Then this is followed with a two dimensional test case, where difference between the single and the multi region approach is visualized, and concluded with the implementation of current source dipoles in spherical geometries.

3.4.1 Single Region and Multi Region Approach in Comparison

To compare the single and the multi region approach, a one-dimensional domain and a two-dimensional rectangular domain are tested. The analytical solution to the one-dimensional problem is given in the appendix. Each test geometry exists of two subdomains Ω_1 , Ω_2 with differing, but constant conductivity

$$\sigma(\mathbf{x}) = \begin{cases} \sigma_1, & \mathbf{x} \in \Omega_1, \\ \sigma_2, & \mathbf{x} \in \Omega_2. \end{cases}$$

One-Dimensional Region with Two Domains of Constant Conductivity

The test domain Ω ranges from $x = 0$ to 1, whereas subdomain Ω_1 is within the limits $[0.3, 0.7]$ and the second subdomain is determined by $\Omega_2 = \Omega \setminus \Omega_1$. Within this test, two different ratios of conductivity, $\frac{\sigma_1}{\sigma_2} = \frac{2}{1}$ and $\frac{\sigma_1}{\sigma_2} = \frac{10}{1}$, were tested. These ratios are motivated by the average conductivity ratios of white and grey matter, i.e. 2, as well as skull and cortex, i.e. 10.

The results for the single region approach, Figure 3.5, show declining accuracy for higher ratios of conductivity. This, however, is caused by the approximation of the derivative of the unsmoothed conductivity field at the discontinuities. In contrast the multi region approach delivers the expected results, see Figure 3.4.

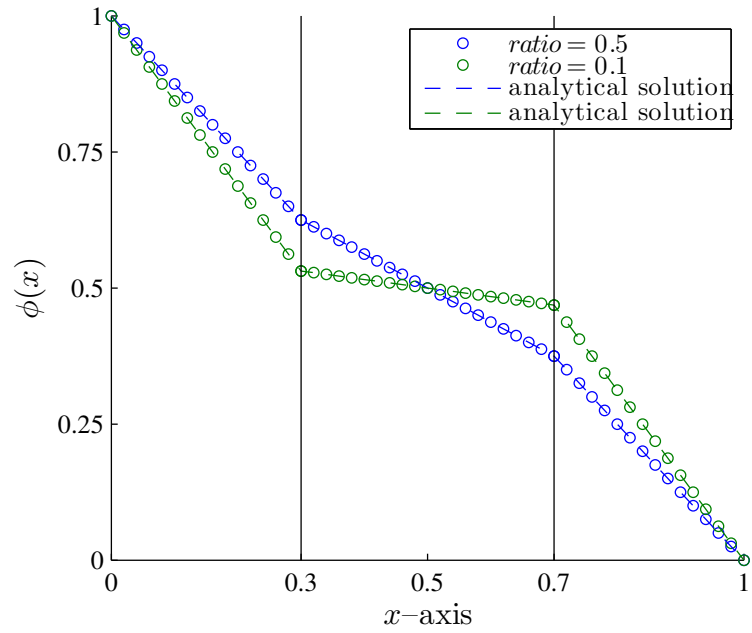


Figure 3.4: Multi region approach with conductivity ratios: $\frac{\sigma_1}{\sigma_2} = 1$, $\frac{\sigma_1}{\sigma_2} = 10$

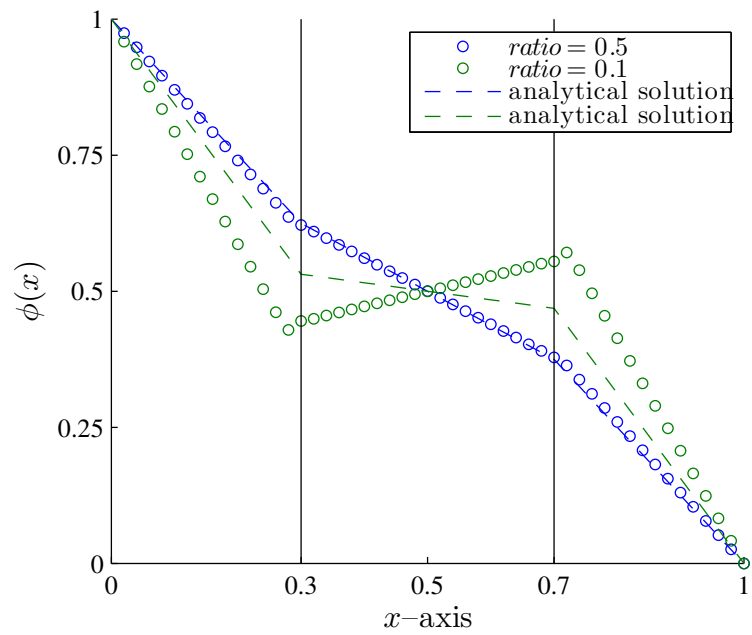


Figure 3.5: Single region approach with conductivity ratios: $\frac{\sigma_1}{\sigma_2} = 1$, $\frac{\sigma_1}{\sigma_2} = 10$

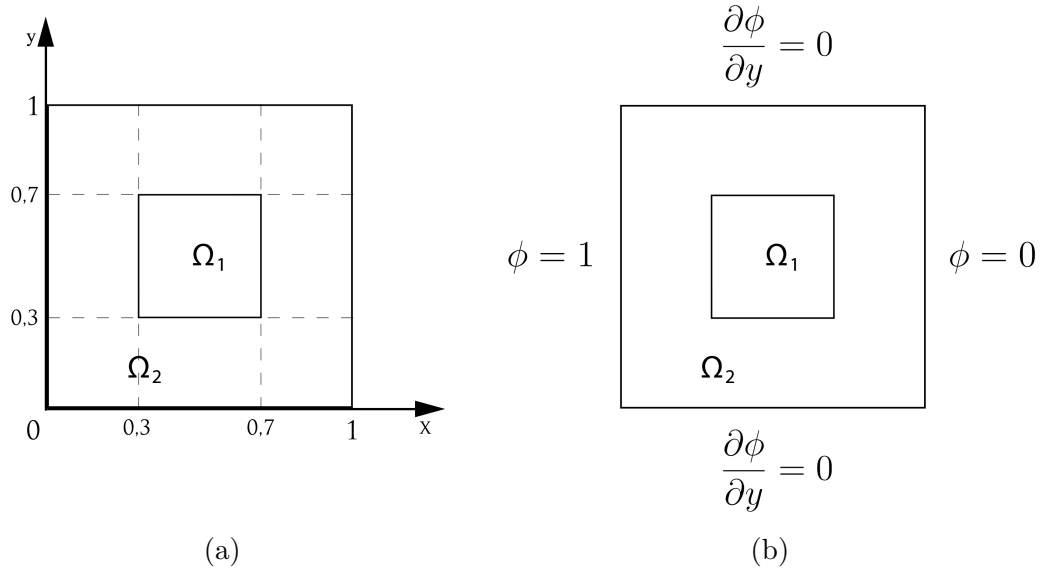


Figure 3.6: Subdomains Ω_1 and Ω_2 with constant conductivity values σ_1 and σ_2 , respectively. (a) shows the subdomains in Cartesian coordinates and (b) the boundary conditions

Two Rectangular Domains with Constant Conductivity in Two Dimensions Now consider a region Ω , also ranging from 0 to 1 in x and y direction, with two rectangular domains Ω_1 and Ω_2 . Here Ω_1 reaches from 0.3 to 0.7 in both directions and, again, $\Omega_2 = \Omega \setminus \Omega_1$, see Figure 3.6a. Both domains possess differing values of conductivity σ_1 , σ_2 and the boundary conditions, see Figure 3.6b, are

$$\phi(0, y) = 0, \quad \phi(1, y) = 1, \quad \frac{\partial \phi(x, 0)}{\partial y} = 0, \quad \frac{\partial \phi(x, 1)}{\partial y} = 0.$$

The results are shown in Figure 3.7 in terms of equipotential lines of the electrical potential ϕ . What can be noticed, is that for a higher ratio of conductivity the inner subdomain Ω_1 gets more and more visible. However for the single region approach and a conductivity ratio $\frac{\sigma_1}{\sigma_2} = 10$ closed equipotential lines occur. This would point towards sources and sinks inside the domain, which must not exist, since the source term $s(\mathbf{x}) = 0$.

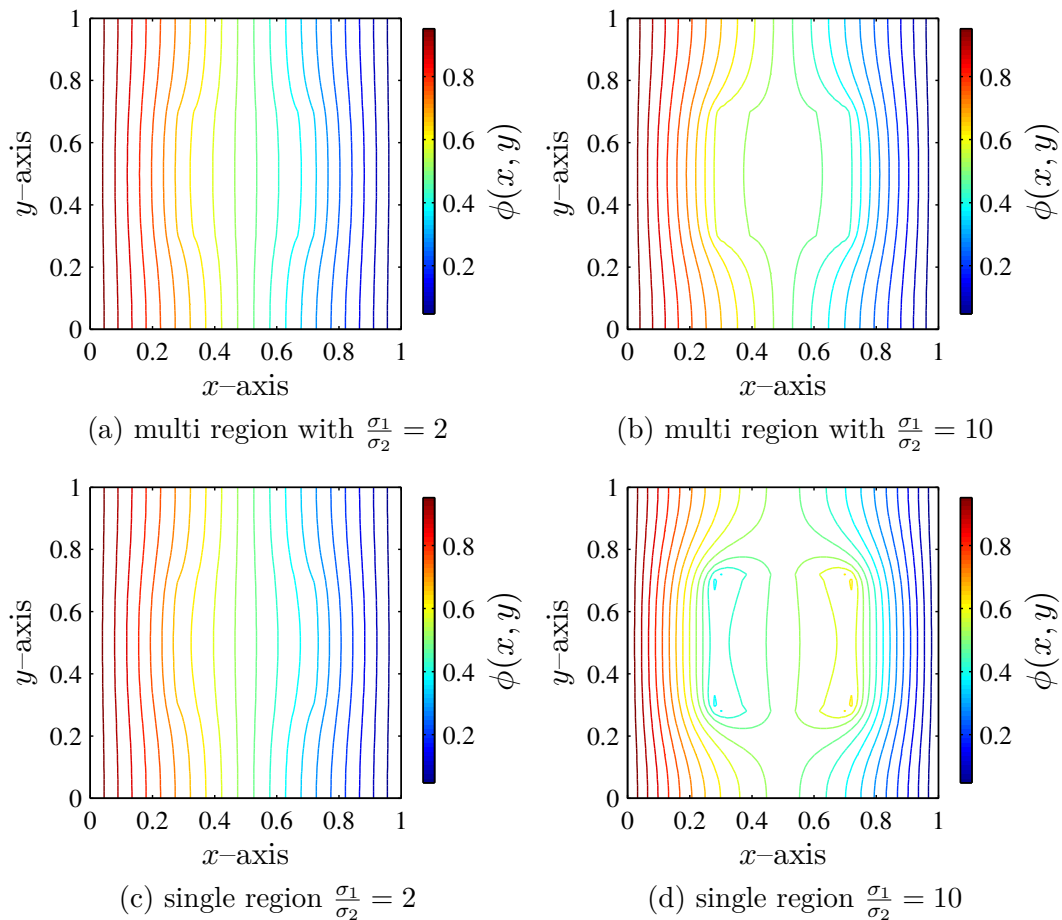


Figure 3.7: Equipotential lines of the electric potential for the single as well as the multi region approach and two ratios of conductivity $\frac{\sigma_1}{\sigma_2} = 2$, $\frac{\sigma_1}{\sigma_2} = 10$.

3.4.2 Multi Region in 3D Spherical Geometries

A single sphere, centred at $(0, 0, 0)$ with radius $R = 0.7$, was implemented inside a cubical region Ω ranging from -1 to 1 in every direction. Following the notation of the two-dimensional rectangular domain, the whole domain is split into two subdomains with constant values of conductivity

$$\Omega = \begin{cases} \Omega_1 & \forall |\mathbf{x}| \leq R, \\ \Omega_2 & \forall |\mathbf{x}| \geq R. \end{cases}$$

The ratio $\frac{\sigma_1}{\sigma_2}$ is always kept to 10. Three models were deployed, one without any source term, another one with an inserted ideal current source dipole, see section 3.3.2, and the last one with a physical current source dipole as described in section 3.3.2.

Sphere with Vanishing Source Term Dirichlet boundary conditions are imposed at the yz -plane at $x = 1$ and $x = -1$

$$\phi(-1, y, z) = 1, \quad \phi(1, y, z) = 0,$$

Neuman boundary conditions at every remaining boundary.

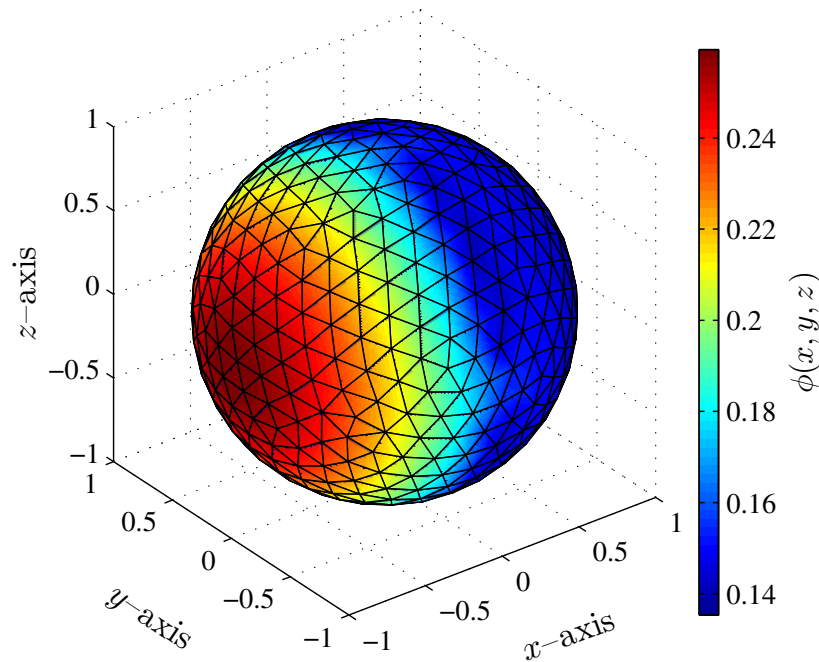


Figure 3.8: Domain Ω with subdomains Ω_i of constant coefficients σ_i . Outside Ω , $\sigma = 0$

The results are as expected, they deliver a linear potential gradient in x -direction, very similar to the result in one dimension.

Sphere Including an Ideal Current Source Dipole For an ideal current source dipole, Neuman boundary conditions are imposed at all boundaries, since the flux through the skin of the head has to be zero [23]. The current source dipole moment is $\mathbf{I}_d^{ideal} = (-1, -1, 1)^T$ at the position $\mathbf{r}_d = (-0.1, -0.1, 0.1)^T$. The result is shown in Figure 3.9 and is consistent with the expected result, cf. [17].

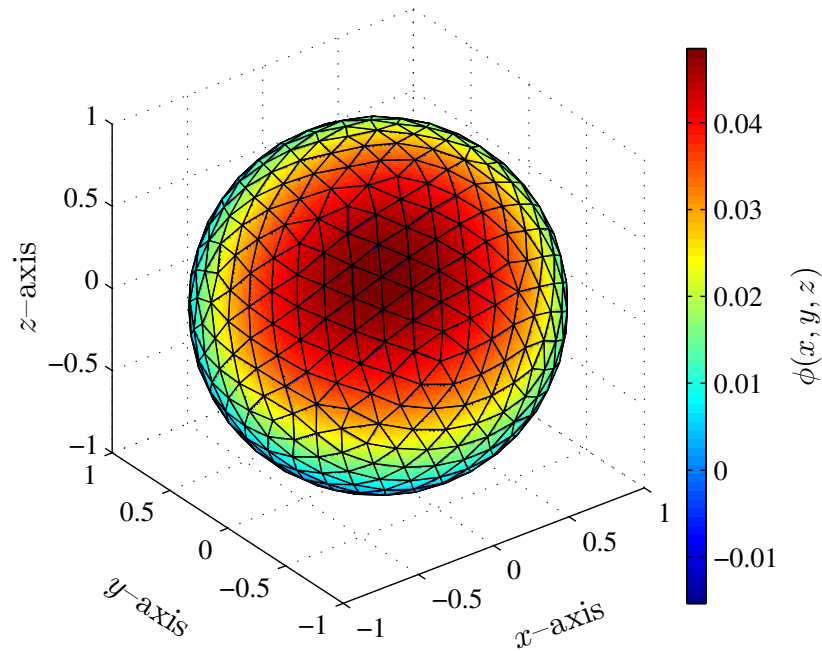


Figure 3.9: Domain Ω with subdomains Ω_i of constant coefficients σ_i . Outside Ω , $\sigma = 0$

Sphere Including an Physical Current Source Dipole The physical current source dipole is also implemented with Neuman boundary conditions at each boundary. The location of the source is chosen to be at $\mathbf{r}_{so} = (0, 0, 0)^T$ and the sink is at $\mathbf{r}_{si} = (-0.2, -0.2, 0.2)^T$. Therefore the distance vector is $\mathbf{d} = (-0.2, -0.2, 0.2)^T$. Moreover the magnitude of the inserted source and the sink is set to $|I_{so}| = |I_{si}| = I_p = 5 \text{ A}$. This leads to an analogous current source dipole model, since the physical and the ideal current source dipole moment are similar $\mathbf{I}_d^{physical} = \mathbf{d} * I_p = (-1, -1, 1)^T$. Figure 3.10 shows the obtained result, which differs only slightly compared to Figure 3.9.

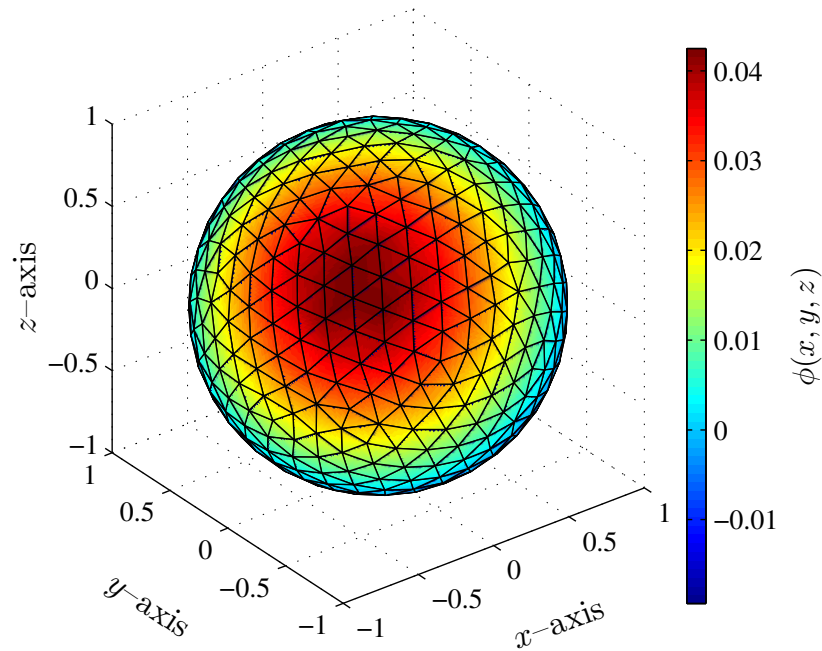


Figure 3.10: Domain Ω with subdomains Ω_i of constant coefficients σ_i . Outside Ω , $\sigma = 0$

3.5 MRI Data Segmentation with Freesurfer

The MRI raw data, shown in Figure 2.4, have to be segmented. Therefore the open source image analysis suite Freesurfer has been used [25],[26],[27]. It is documented and freely available for download online at <http://surfer.nmr.mgh.harvard.edu/>. The segmentation was done with two different routines, the recon-all routine and the mri-watershed routine. Whereas the recon-all routine provides segmentation up to subcranial regions, the mri-watershed routine delivers a rougher but much more suitable one, because it distinguishes mainly cortex, the cerebrospinal fluid, skull and skin. Several geometries were obtained. For exemplary purpose a geometry of the cortex is shown in Figure 3.12 and of the skull in Figure. 3.11

First tests of the forward model framework, however, did not deliver the expected results. Further steps will have to be taken into account to tune the algorithms for the increased complexity of the geometry. Also, generalizing the developed method to complex geometries does not constitute any conceptual problems.

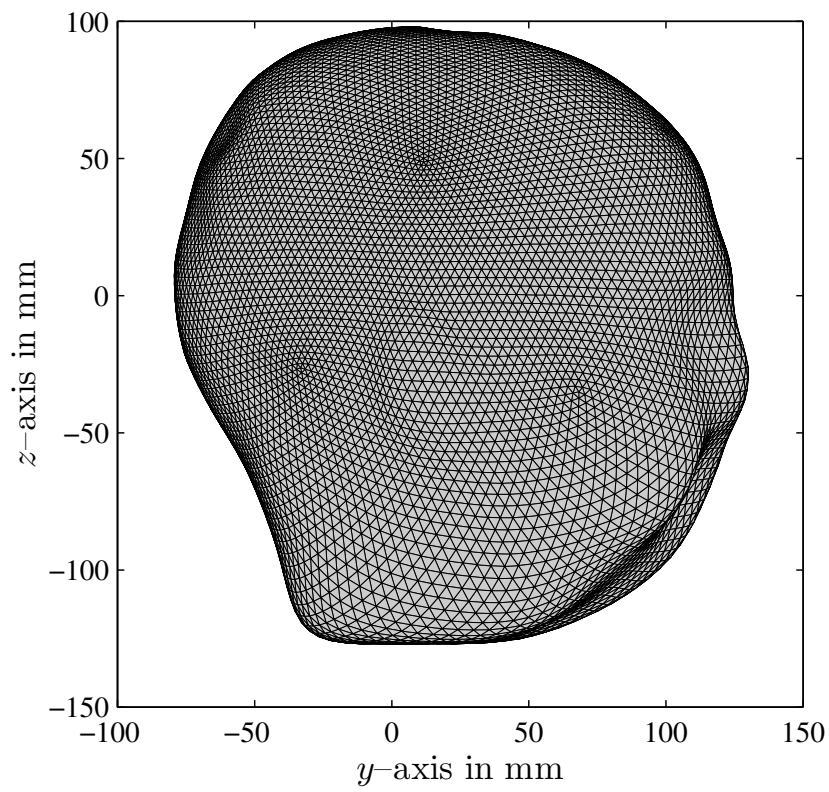


Figure 3.11: Complex geometry of the skull surface

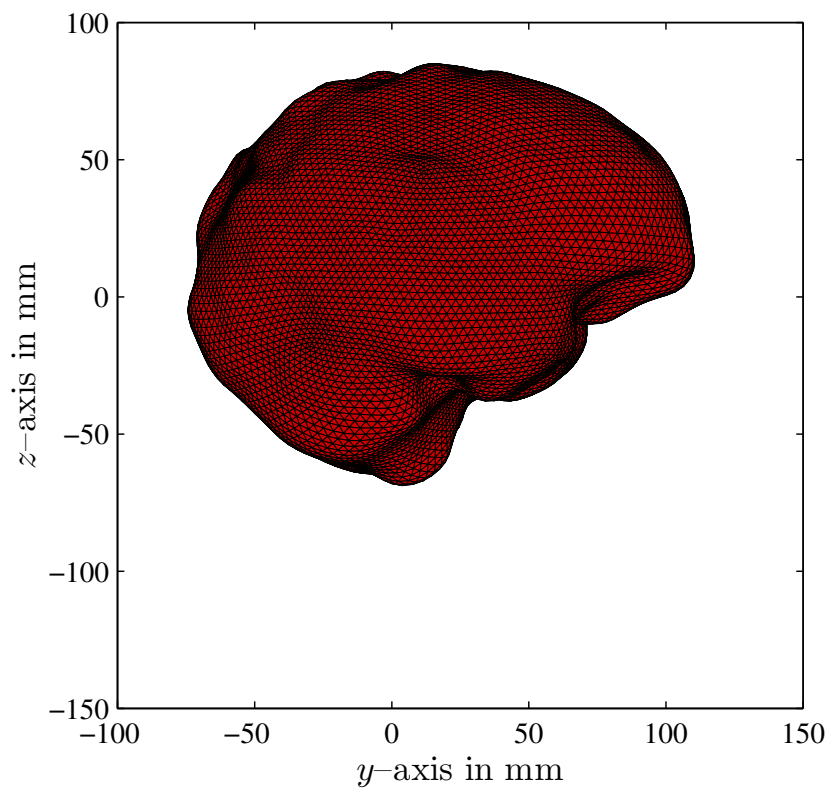


Figure 3.12: Complex geometry of the brain surface

Chapter 4

Conclusion and Outlook

In this thesis the DCPSE Operator has been utilized to solve the PDE for the electric potential in domains consisting of subdomains with different, nevertheless constant conductivities. Two methods, the single and the multi region approach, have been tested, whereas the multi region technique performed with far superior accuracy. This is strongly related to the unsmoothed conductivity field in the single region approach, which should be included in next tests, because it is far more computationally efficient than its multi region counterpart.

The implementation of the current source dipole was successful. Albeit this accomplishment, it would be beneficial to continue with further studies, especially on validating the results with analytic solutions of such models. Such solutions exist, but they are very complex. In conclusion, the results are very promising, although more effort has to be put in the development of the framework on to realistic head models.

This marks the first steps towards a meshfree particle simulation of the forward model and future work can involve a more sophisticated physical model, containing the anisotropic conductivity of the brain tissue and more realistic dipole models like a weighted current source distribution. It also can focus on parallelization of the framework, e.g. with the use of pseudo-time step schemes, since in this approach a global LSE has to be solved. The biggest goal, however, should be to use the MRI-EEG correlation data set to validate the forward model.

Appendix A

Analytic Solution for a Region with Three Subdomains of Constant Conductivity

Consider the PDE

$$\nabla\sigma(x) (\nabla\phi(x)) = 0$$

in a 1-dimensional domain Ω consisting of three subdomains, Ω_1 ranging from x_0 to x_1 , Ω_2 from x_1 to x_2 and Ω_3 from x_2 to x_3 . For each of these subdomains the value of conductivity, $\sigma_1, \sigma_2, \sigma_3$, can be different, but has to be constant over the whole subdomain. Furthermore the boundary conditions,

$$\phi(x_0) = C, \quad \phi(x_3) = K,$$

exist. Therefore the assumption to split the potential into three solutions, one for each subdomain,

$$\phi(x) = \begin{cases} \phi_1(x), & x \in \Omega_1, \\ \phi_2(x), & x \in \Omega_2, \\ \phi_3(x), & x \in \Omega_3, \end{cases}$$

can be made, cf. [7], and leads to three PDEs

$$\sigma_i \Delta \phi_i(x) = 0, \quad x \in \Omega_i. \tag{A.1}$$

Since ϕ has to be continuous and the flux through each interface may not change, one has to consider following interface conditions

$$\begin{aligned} \phi_i(x_i) &= \phi_{i+1}(x_i), \\ \sigma_i \frac{d\phi_i(x)}{dx} \Big|_{x=x_i} &= \sigma_{i+1} \frac{d\phi_{i+1}(x)}{dx} \Big|_{x=x_i}. \end{aligned}$$

Also, regarding Eq. A.1, the form of the ϕ_i is supposed to be

$$\phi_i(x) = a_i x + b_i, \quad x \in \Omega_i.$$

The six equations to determine the six unknowns are the two boundary conditions and the four interface conditions, two for each interface. Solving the arising LSE, the coefficients are set by these equations

$$\begin{aligned} a_1 &= \frac{K - C}{(x_1 - x_0) - \frac{\sigma_1}{\sigma_2}(x_1 - x_2) - \frac{\sigma_1}{\sigma_3}(x_2 - x_3)} \\ a_2 &= \frac{\sigma_1}{\sigma_2} a_1 \\ a_3 &= \frac{\sigma_2}{\sigma_3} a_2 \\ b_1 &= C - x_0 a_1 \\ b_2 &= K - x_2 a_2 - (x_2 - x_3) a_3 \\ b_3 &= K - x_3 a_3 \end{aligned}$$

For the parameters $C = 1$, $K = 0$, $x_0 = 0$, $x_1 = 0.3$, $x_2 = 0.7$, $x_3 = 1$ and moreover $\sigma_1 = \sigma_3$, this directly yields for any ratio σ_1/σ_2

$$\begin{aligned} a_1 &= \frac{-1}{0.4 \frac{\sigma_1}{\sigma_2} + 0.6} \\ a_2 &= \frac{\sigma_1}{\sigma_2} a_1 \\ a_3 &= a_1 \\ b_1 &= 1 \\ b_2 &= (x_1 - x_0) a_1 - x_1 a_2 + C \\ b_3 &= -a_3 \end{aligned}$$

Bibliography

- [1] H. Berger, *Über das Elektrenkephalogramm des Menschen*, Archiv für Psychiatrie und Nervenkrankheiten 87.1 (Dec. 1929), pp. 527–570.
- [2] S. Baillet, J.C. Mosher, and R.M. Leahy, *Electromagnetic brain mapping*, IEEE Signal Processing Magazine 18.6 (2001), pp. 14–30.
- [3] M. Hämäläinen, R. Hari, R. J. Ilmoniemi, J. Knuutila, and O. V. Lounasmaa, *Magnetoencephalography—theory, instrumentation, and applications to noninvasive studies of the working human brain*, Reviews of Modern Physics 65.2 (Apr. 1993), pp. 413–497.
- [4] Cross Section of the Human Brain, Retrieved on 20 November. URL: <http://www.headinjury.com/brainmapx.htm>.
- [5] S. Zschocke and H.-C. Hansen, *Klinische Elektroenzephalographie*. Springer, 2012.
- [6] Neuron Current Flow, Retrieved on 8 November. URL: <http://www.canadameg-consortium.org/EN/MegBaillet2>.
- [7] J. Jackson, *Klassische Elektrodynamik*. De Gruyter, 2014.
- [8] T.E. Katila, *Round table. On the current multipole presentation of the primary current distributions*, Il Nuovo Cimento D 2.2 (Mar. 1983), pp. 660–664.
- [9] J.C. de Munck, B.W. van Dijk, and H. Spekreijse, *Mathematical dipoles are adequate to describe realistic generators of human brain activity*. IEEE transactions on bio-medical engineering 35.11 (Nov. 1988), pp. 960–6.
- [10] E. Wintermantel and S.-W. Ha, *Medizintechnik Life Science Engineering*. Berlin, Heidelberg: Springer, 2008.
- [11] B. Marincek, D. Weishaupt, and V.D. Köchli, *How Does MRI Work? An Introduction to the Physics and Function of Magnetic Resonance Imaging*. Springer, 2006.
- [12] M.L. Lipton, *MRI Physics: A User’s Guide to Principles, Technology, and Applications*. Springer, 2010.

- [13] Magnetic Moment in MRI, Retrieved on 27 November. URL: <http://www.iomonitoring.org/mrphysics.htm>.
- [14] Spin Orientation in MRI, Retrieved on 27 November. URL: <http://www.mikepuddephat.com/Page/1603/Principles-of-magnetic-resonance-imaging>.
- [15] EEG Electrodes, Retrieved on 5 November. URL: http://www.inapic.uzh.ch/studienteilnahme/neurowissenschaftliche-verfahren/eeg%5C_de.html.
- [16] N. von Ellenrieder, C.H. Muravchik, and A. Nehorai, *A meshless method for solving the EEG forward problem*. IEEE transactions on bio-medical engineering 52.2 (Feb. 2005), pp. 249–57.
- [17] G. Ala and E. Francomano, *A multi-sphere particle numerical model for non-invasive investigations of neuronal human brain activity*, enProgress In Electromagnetics Research Letters 36 (2013), pp. 143–153.
- [18] P. Degond and S. Mas-Gallic, *The weighted particle method for convection-diffusion equations. I. The case of an isotropic viscosity*, Mathematics of Computation 53.188 (1989), pp. 485–485.
- [19] O. Awile, *A Domain-Specific Language and Scalable Middleware for Particle-Mesh Simulations on Heterogeneous Parallel Computers*, Diss. ETH No. 20959 (2013).
- [20] J.D. Eldredge, A. Leonard, and T. Colonius, *A General Deterministic Treatment of Derivatives in Particle Methods*, Journal of Computational Physics 180.2 (Aug. 2002), pp. 686–709.
- [21] B. Schrader, S. Reboux, and I.F. Sbalzarini, *Discretization correction of general integral PSE Operators for particle methods*, Journal of Computational Physics 229.11 (June 2010), pp. 4159–4182.
- [22] B. Schrader, *Discretization-corrected PSE operators for adaptive multiresolution particle methods*, Diss. ETH No. 19566 (2011).
- [23] Carsten H. Wolters, *Influence of Tissue Conductivity Inhomogeneity and Anisotropy on EEG/MEG based Source Localization in the Human Brain*, (2003).
- [24] J. Sarvas, *Basic mathematical and electromagnetic concepts of the biomagnetic inverse problem*, Physics in Medicine and Biology 32.1 (Jan. 1987), pp. 11–22.

- [25] A.M. Dale, B. Fischl, and M.I. Sereno, *Cortical surface-based analysis. I. Segmentation and surface reconstruction*. NeuroImage 9.2 (Feb. 1999), pp. 179–94.
- [26] A.M. Dale and M.I. Sereno, *Improved Localizadon of Cortical Activity by Combining EEG and MEG with MRI Cortical Surface Reconstruction: A Linear Approach*. enJournal of cognitive neuroscience 5.2 (Jan. 1993), pp. 162–76.
- [27] R.S. Desikan et al., *An automated labeling system for subdividing the human cerebral cortex on MRI scans into gyral based regions of interest*. NeuroImage 31.3 (July 2006), pp. 968–80.

Appendix B

Selbstständigkeitserklärung

Hiermit versichere ich, dass ich die vorliegende Arbeit ohne unzulässige Hilfe Dritter und ohne Benutzung anderer als der angegebenen Hilfsmittel angefertigt habe. Die aus fremden Quellen direkt oder indirekt übernommenen Gedanken sind als solche kenntlich gemacht. Die Arbeit wurde bisher weder im Inland noch im Ausland in gleicher oder ähnlicher Form einer anderen Prüfungsbehörde vorgelegt.

Fabian Multrus Dresden, 19.12.2014